

DATA-DRIVEN FRACTURE MECHANICS

P. CARRARA*, L. DE LORENZIS, L. STAINIER, AND M. ORTIZ

ABSTRACT. We present a new data-driven paradigm for variational brittle fracture mechanics. The fracture-related material modeling assumptions are removed and the governing equations stemming from variational principles are combined with a set of discrete data points, leading to a model-free data-driven method of solution. The solution at a given load step is identified as the point within the data set that best satisfies either the Kuhn-Tucker conditions stemming from the variational fracture problem or global minimization of a suitable energy functional, leading to data-driven counterparts of both the local and the global minimization approaches of variational fracture mechanics. Both formulations are tested on different test configurations with and without noise and for Griffith and R-curve type fracture behavior.

CONTENTS

1. Introduction	2
2. Classical fracture mechanics	3
2.1. Equilibrium of a cracked elastic solid	4
2.2. Equilibrium of a cracked elastic solid connected to a testing machine	6
3. Data-driven fracture mechanics	8
3.1. Data representation	8
3.2. Computational procedure	9
3.3. Numerical implementation	10
4. Numerical examples	13
4.1. Griffith fracture	15
4.2. R-curve fracture	24
4.3. Bimaterial DCB	27
4.4. Tapered DCB	31
4.5. Convergence	32
5. Summary and concluding remarks	37
Acknowledgements	38
References	38
Appendix A. Compliance for the tapered DCB	39

Key words and phrases. data-driven computational mechanics, fracture mechanics, model-free, numerical modeling.

*Corresponding author pcarrara@ethz.ch.

1. INTRODUCTION

Data-driven techniques rooted in data science and machine learning recently experienced a tremendous development and a boost of applications in many fields such as finance, advertising and marketing, to create predictive models based on large sets of discrete data [1]. Related approaches were applied since the late '80s to mechanics problems but were restricted to pre- or post-processing procedures, with the aim of identifying unknown parameters in pre-defined material constitutive laws or for design optimization [2, 3, 4], whereas the solution of the mechanics boundary value problems followed the conventional lines.

More recently, the novel paradigm of model-free data-driven computational mechanics was advocated [5]. The main idea is that boundary value problems in mechanics are based upon two types of relationships: an epistemic and certain set of basic conservation laws (e.g., energy balance, equilibrium, compatibility) and an empirical and uncertain set of material constitutive equations [5]. The uncertainty of the latter stems from the attempt to distillate analytical models from collected data, with an unavoidable manipulation of the information [6]. In this process, uncertain assumptions on the characteristics of the constitutive model are introduced to obtain objective functions that are calibrated using the collected data, also affected by uncertainty. The consequent interaction between these two sources of uncertainty is hardly predictable and can be avoided by directly replacing the classical constitutive relationships with information supplied by discrete raw observations.

The data-driven solver in [5] assigns to each material state the point in the available data set closest to the subset of points fulfilling compatibility and equilibrium. Subsequent extensions were proposed to geometrically nonlinear elasticity [7, 8], and elastodynamics [9]. Further developments include a maximum entropy scheme increasing robustness with respect to outliers [10], and the reformulation of the problem in the framework of mixed-integer quadratic optimization [11]. Based on the approach in [5], a new methodology to identify material parameters and stresses in experimental testing based on digital image correlation was developed in [12, 13]. Alternative data-driven formulations [14, 15] seek to reconstruct a constitutive manifold from data using manifold learning methods. In the case of elasticity, the goal is to use data to identify a suitable approximation of the strain energy density functional.

Extensions of the data-driven formulation to inelastic materials have been considered by Eggersmann *et al.* [16]. The fundamental challenge is to account for the history dependence of the material without modeling assumptions such as an *ad hoc* choice of internal variables. Eggersmann *et al.* [16] investigate three representational paradigms for the evolving material data sets: i) materials with memory, i. e., conditioning the material data set to the past history of deformation; ii) differential materials, i. e., conditioning the

material data set to short histories of stress and strain; and iii) history variables, i. e., optimally identifying variables encoding as much information as possible about history dependence in stress-strain data. In this latter vein, a particular choice of internal variable, namely, the plastic-strain rate, has been considered in [17]. Despite these advances, the extension of the model-free data-driven approach to dissipative inelastic behavior remains a largely open and non-trivial challenge.

In this paper, we propose a data-driven approach to the solution of the rate independent fracture problem in brittle materials. This class of problems is particularly suited to be adapted to the model-free data-driven paradigm since the natural choice for the history variable is the crack extension, which is easy to measure experimentally. We assume a known linear elastic constitutive behavior of the material and focus on the data-driven solution of the fracture problem. Along the same lines as in [5], we remove the fracture-related material modeling assumptions and let the fracture constitutive behavior be fully encoded in a discrete set of material data. In addition, we derive the epistemic and certain set of conservation laws from variational principles. In the variational formulation of the fracture problem, we consider both the stationarity condition of the free energy, i. e., a solution based on metastability or local stability [18], which is the closest to Griffith's view of fracture, and a solution based on global stability in the spirit of [19]. The solution at a given load step is identified as the point within the data set that best fulfills either stationarity or global minimization of the free energy, leading to the data-driven counterparts of both the local and the global minimization approaches.

While this paper focuses on the simplest possible setting to best clarify the concepts, several extensions are possible and will be addressed in future research. They include the detailed discussion of different crack modes and the prediction of crack paths in the general two- and three-dimensional case, as well as rate-dependent and ductile fracture and many other more complex cases.

The remainder of this paper is structured as follows. In Sect. 2 standard rate-independent fracture mechanics is briefly recalled along with its variational setting in terms of both local and global minimization of the free energy. The data-driven counterparts are formulated in Sect. 3, where also the main aspects of the numerical implementation are described. Sect. 4 presents some numerical examples, where standard and data-driven formulations are tested on different setups with and without noise, for Griffith and R-curve type fracture behavior. Conclusions are drawn in Sect. 5.

2. CLASSICAL FRACTURE MECHANICS

Throughout this work, we are concerned with the problem of modeling the growth of cracks in elastic materials. In order to focus attention on how data-driven concepts apply to fracture mechanics, we consider the simplest

possible case of a solid with a known linearly elastic constitutive behavior, in which the crack set can be characterized by a single length parameter a .

2.1. Equilibrium of a cracked elastic solid. Crack growth is an inelastic process in which the crack configuration evolves according to kinetics and is driven by energetic forces. In order to exhibit the structure of the theory in its simplest form, we adopt a compliance representation of the energy and assume planar rate-independent crack growth under mode I loading. Under these conditions, the configuration of the crack is described by the single variable a , which plays the role of a state variable, the loading by an effective force P and the deformation by a conjugate effective displacement Δ . At equilibrium P and Δ necessarily bear a linear relation of the form

$$(1) \quad \Delta = C(a)P$$

where $C(a)$ is the crack-length-dependent *compliance* of the solid (Fig. 1a). Throughout this paper we assume the compliance function to be exactly known.

We assume displacement control and formulate the equilibrium problem as follows. Suppose the solid has an initial crack of length a_0 , and it is imparted a prescribed opening displacement Δ (Fig. 1a). Our goal is to determine the equilibrium crack length $a^*(\Delta, a_0)$, where we postulate $a^* \geq a_0$ due to irreversibility, and the corresponding load P (Fig. 1a). More generally, within an incremental displacement-controlled loading process, we may want to determine the incremental behavior of the system; i.e., for given Δ_{k+1} at time t_{k+1} and a_k at time t_k , determine $a_{k+1}(\Delta_{k+1}, a_k)$, with $a_{k+1} \geq a_k$ due to irreversibility, and the corresponding load P_{k+1} . Note that the quantity a_k plays here the role of a history variable.

Both the equilibrium and the incremental problem can be characterized variationally by means of energy dissipation principles. As follows, we formulate the equilibrium problem. We introduce the elastic strain energy of the solid

$$(2) \quad E = \frac{\Delta^2}{2C(a)},$$

which has the properties

$$(3) \quad P = \frac{\partial E}{\partial \Delta}(\Delta, a), \quad G = -\frac{\partial E}{\partial a}(\Delta, a),$$

where G is known as the energy release rate. Combining (2) and (3b) gives

$$(4) \quad G = \frac{\Delta^2}{2C^2(a)} \frac{dC}{da},$$

which provides a shortcut to compute G known as compliance method. Let us now introduce the free energy

$$(5) \quad F(\Delta, a) = E(\Delta, a) + F_R(a),$$

where the resistance term $F_R(a)$ has the property that

$$(6) \quad G_R(a) = \frac{dF_R(a)}{da},$$

defines the resistance curve in terms of energy release rates. For the solution of the problem based on the variational principle of free energy minimization we have two options.

One possibility is to look for the value of crack length which corresponds to the *global minimum* of the free energy, i. e.,

$$(7) \quad F(\Delta, a^*) \leq F(\Delta, a) \quad \forall a \geq a_0,$$

or

$$(8) \quad a^*(\Delta, a_0) = \operatorname{argmin} \{F(\Delta, a) : a \geq a_0\}.$$

Another possibility is to look for the value of crack length which corresponds to a *local minimum* of the free energy, i. e., to look for a^* such that there exists $h > 0$ satisfying

$$(9) \quad F(\Delta, a^*) \leq F(\Delta, a^* + a - a^*) \quad \forall a \geq a_0, |a - a^*| \leq h,$$

i. e., for each $a \geq a_0$ in the *neighborhood* of a^* . A first-order Taylor series expansion of the right-hand side, along with (3b) and (6), leads to

$$(10) \quad [G(\Delta, a^*) - G_R(a^*)](a - a^*) \leq 0 \quad \forall a \geq a_0.$$

There are two possibilities to satisfy this condition, namely

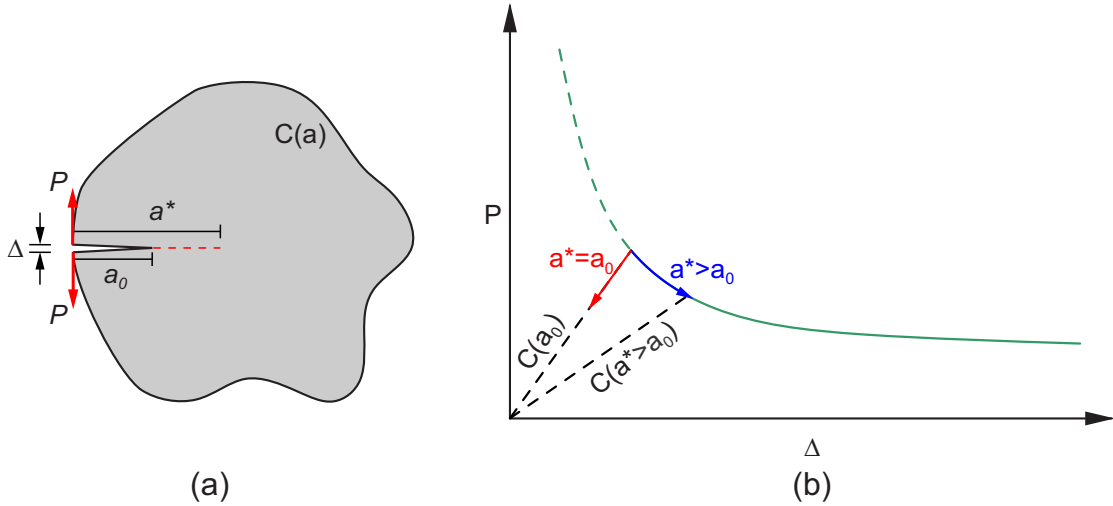


FIGURE 1. (a) Sketch of the equilibrium problem and (b) schematic representation of the equilibrium curve exhibiting loading/elastic unloading behavior.

- for $a^* > a_0$, $a - a^*$ can have any sign. Hence, in order to satisfy (10), it must be $G(\Delta, a^*) - G_R(a^*) = 0$;
- for $a^* = a_0$, it can only be $a - a^* \geq 0$, so that (10) gives $G(\Delta, a^*) - G_R(a^*) \leq 0$.

These conditions can be collected in Kuhn-Tucker form as

$$(11) \quad \begin{aligned} a^* - a_0 &\geq 0 \\ G(\Delta, a^*) - G_R(a^*) &\leq 0 \\ [G(\Delta, a^*) - G_R(a^*)](a^* - a_0) &= 0. \end{aligned}$$

Evidently, these relations reduce to the Griffith criterion when $G_R(a) = G_c = \text{constant}$.

Global and local minimization obviously deliver the same solution if the free energy is a convex function of a . Otherwise, it is known in the literature that the two options in general deliver different results. In particular, the local minimality principle forbids the evolution between states that are separated by energetic barriers and tries to find the next equilibrium state in the neighborhood of the current state. Conversely, globally stable processes can evolve to conditions that are energetically more favorable but separated by arbitrarily large energetic barriers violating the causality principle and leading to anticipated jumps. This ultimately leads to a globally stable states domain that is smaller compared to the local counterpart, see [18].

Inserting $a^*(\Delta, a_0)$ obtained either from (8) or from (11) into the equilibrium relation (3a), we obtain

$$(12) \quad P = \frac{\partial E}{\partial \Delta}(\Delta, a^*(\Delta, a_0)),$$

which characterizes all possible (P, Δ) pairs attainable by the system given a_0 . Hence, for a given Δ it is immediate to find P . We expect the curve defined by (12) to exhibit loading-unloading behavior, with elastic unloading occurring when $a^*(\Delta, a_0) = a_0$, i. e., under conditions of crack arrest, and loading when $a^*(\Delta, a_0) > a_0$, i. e., under conditions of crack growth (Fig. 1b).

2.2. Equilibrium of a cracked elastic solid connected to a testing machine. Suppose, more generally, that the solid is connected to a testing machine of compliance C_M . Then, the opening displacement Δ and the load are related as

$$(13) \quad \Delta_T = \Delta + C_M P,$$

where Δ_T is a time-dependent control opening displacement. Other loading devices result in different load-displacement relations and may involve

different control parameters, but the simple linear device (13) suffices to illustrate the concept. The elimination of P between (3a) and (13) delivers

$$(14) \quad \Delta = \frac{C(a)}{C(a) + C_M} \Delta_T.$$

Once again we formulate the equilibrium problem. The solid has an initial crack of length a_0 , and it is subjected by the testing machine to a prescribed opening displacement Δ_T . Our goal is to determine the equilibrium crack length $a^*(\Delta_T, a_0)$, where we postulate $a^* \geq a_0$ due to irreversibility, and the corresponding load P and opening displacement Δ . In fact, we first determine $a^*(\Delta, a_0)$ to leverage the results in Sect. 2.1, and then show how one can directly determine $a^*(\Delta_T, a_0)$.

In this case one can introduce a mixed variational principle, as follows. Define the function

$$(15) \quad \Phi(\Delta, P, a) = E(\Delta, a) + F_R(a) - \frac{C_M}{2} P^2 - P(\Delta - \Delta_T).$$

It is straightforward to verify that the Euler-Lagrange equations of the saddle-point problem

$$(16) \quad \min_{\Delta} \min_{a \geq a_0} \max_P \Phi(\Delta, P, a),$$

are indeed (12), (13) and the Kuhn-Tucker conditions (11). The latter conditions obviously only hold if local minimization is pursued; alternatively, the direct global minimization of (15) with respect to $a \geq a_0$ must be carried out. Evidently, once, for a given Δ_T , $a^*(\Delta, a_0)$ is determined by either global or local minimization, the new state (P, Δ) of the system must satisfy relations (12) and (13) simultaneously, i. e., it must lie at the intersection of the curves defined by (12) and (13). This defines automatically P and Δ .

A more direct way to proceed is the following. By substituting (3a) and (13) into (15), the following reduced function is obtained

$$(17) \quad \tilde{\Phi}(\Delta_T, a) = \tilde{E}(\Delta_T, a) + F_R(a),$$

with

$$(18) \quad \tilde{E} = \frac{1}{2} \frac{\Delta_T^2}{C(a) + C_M},$$

which can then be directly minimized (globally or locally) with respect to a at given Δ_T and a_0 . Global minimization delivers

$$(19) \quad a^*(\Delta_T, a_0) = \operatorname{argmin} \left\{ \tilde{\Phi}(\Delta_T, a) : a \geq a_0 \right\},$$

whereas local minimization leads to

$$\begin{aligned}
(20) \quad & a^* - a_0 \geq 0 \\
& \tilde{G}(\Delta_T, a^*) - G_R(a^*) \leq 0 \\
& \left[\tilde{G}(\Delta_T, a^*) - G_R(a^*) \right] (a^* - a_0) = 0,
\end{aligned}$$

where $\tilde{G}(\Delta_T, a)$ is obtained from the combination of $G(\Delta, a)$ and (14).

3. DATA-DRIVEN FRACTURE MECHANICS

For most materials, the crack resistance curve is only known through material testing, which results in limited data in the form of point sets. In addition, such data can be noisy. In the spirit of data-driven mechanics [5], we explore the possibility of solving fracture mechanics problems directly from data.

3.1. Data representation. The question now arises of how to characterize fracture by means of data. To this end, we begin by reexamining the classical equilibrium problem of Sect. 2.2 in which $E(\Delta, a)$, $F_R(a)$ and the loading device are exactly known and characterized.

We adopt the viewpoint that a solution is a pair (Δ, P) that simultaneously satisfies compatibility, equilibrium and the material laws. The space of solutions, or *phase space*, is therefore the space \mathcal{Z} of work-conjugate pairs (Δ, P) . Given a_0 , we may identify the subset of \mathcal{Z} ,

$$(21) \quad \mathcal{D} = \{(\Delta, P) : \text{equation (12)}\},$$

as a *material data set* which collects the net sum of our knowledge about the material. Likewise, given Δ_T we may identify the subset of \mathcal{Z} ,

$$(22) \quad \mathcal{E} = \{(\Delta, P) : \text{equation (13)}\},$$

as a *constraint set*, consisting of all points in phase space that are compatible and in equilibrium with the loading machine. Evidently, within this framework the solution set for given a_0 and Δ_T is the intersection $\mathcal{D} \cap \mathcal{E}$, i. e., the collection of points in phase space that are simultaneously in the material and constraint data sets.

Suppose now that the elastic energy $E(\Delta, a)$ is exactly known, e. g., in terms of a fully characterized compliance, whereas the resistance part $F_R(a)$ of the free energy or its derivative $G_R(a)$ is known only from data. Given a crack length a_0 and an opening displacement Δ , the corresponding equilibrium crack length $a^*(\Delta, a_0)$ can be found from the data by either global or local minimization. Within an incremental loading procedure, we compute the equilibrium crack length a_{k+1} for given displacement Δ_{k+1} at time t_{k+1} and crack length a_k at time t_k . This relation in turn defines the material data set,

$$(23) \quad \mathcal{D}_{k+1} = \{(\Delta_{k+1}, P(\Delta_{k+1}, a^*(\Delta_{k+1}, a_k)))\},$$

of all possible opening displacements and loads attainable at time t_{k+1} .

Let \mathcal{E}_{k+1} be the constraint set of points (Δ_{k+1}, P_{k+1}) consistent with the loading device at time t_{k+1} . We define the data-driven solution set at time t_{k+1} as the intersection $\mathcal{D}_{k+1} \cap \mathcal{E}_{k+1}$, i. e., the collection of points in phase space that are simultaneously in the material and constraint data sets.

As in (16), the entire solution $(\Delta_{k+1}, P_{k+1}, a_{k+1})$ can be characterized jointly by means of the saddle point problem

$$(24) \quad \min_{\Delta} \min_{\substack{a \geq a_0 \\ (a, F_R) \in \mathcal{D}_R}} \max_P \left(E(\Delta, a) + F_R - \frac{C_M}{2} P^2 - P(\Delta - \Delta_T) \right),$$

which now entails a discrete minimization over the resistance data set \mathcal{D}_R . If using local minimization with respect to a , $(a, F_R) \in \mathcal{D}_R$ must be substituted by $(a, G_R) \in \mathcal{D}_R$ in (24).

3.2. Computational procedure. A more direct and practical way of proceeding, which mirrors the introduction of the “reduced” function $\tilde{\Phi}$ in Sect. 2.2, is the following.

When using the global minimization approach, the resistance data set \mathcal{D}_R consists of pairs $(\hat{a}_i, \hat{F}_{Ri})$ and minimization is straightforwardly performed as follows: $a^*(\Delta_T, a_0) = \hat{a}_{i^*}$ with

$$(25) \quad i^*(\Delta_T, a_0) = \underset{i}{\operatorname{argmin}} \left\{ \tilde{E}(\Delta_T, \hat{a}_i) + \hat{F}_{Ri} : \hat{a}_i \geq a_0, (\hat{a}_i, \hat{F}_{Ri}) \in \mathcal{D}_R \right\}.$$

Note that $a^*(\Delta_T, a_0)$ follows from a discrete minimization over the point set \mathcal{D}_R and is, therefore, stepwise.

With local minimization, the data set \mathcal{D}_R consists of pairs $(\hat{a}_i, \hat{G}_{Ri})$. Finding $a^*(\Delta_T, a_0)$ requires a little more care. A possible strategy is based on closest-point projection. Here we first determine G_{R0} as the value of \hat{G}_R corresponding to $\hat{a} = a_0$. Then, if the propagation condition is met, i. e., $G_{R0} - \tilde{G}(\Delta_T, a_0) \leq 0$, and for each $(\hat{a}_i, \hat{G}_{Ri})$ pair in the data set with $\hat{a}_i \geq a_0$, we determine the distance to the analytical curve $\tilde{G}(\Delta_T, a)$ as

$$(26) \quad \tilde{d}_i(\Delta_T, a_0) = \min_{a \geq a_0} \left\{ \sqrt{(\hat{a}_i - a)^2 + (\hat{G}_{Ri} - \tilde{G}(\Delta_T, a))^2} \right\},$$

and then compute $a^*(\Delta_T, a_0)$ by minimizing the distance between $\tilde{G}(\Delta_T, a)$ and the resistance data set, as follows: $a^*(\Delta_T, a_0) = \hat{a}_{i^*}$ with

$$(27) \quad i^*(\Delta_T, a_0) = \underset{i}{\operatorname{argmin}} \left\{ \tilde{d}_i(\Delta_T, a_0) : \hat{a}_i \geq a_0, (\hat{a}_i, \hat{G}_{Ri}) \in \mathcal{D}_R \right\}.$$

A second possible strategy for local minimization is based on the best approximation of the third Kuhn-Tucker condition (known as the consistency condition). With this strategy, we compute

$$(28) \quad i^*(\Delta_T, a_0) = \underset{i}{\operatorname{argmin}} \left\{ \left| \left(\tilde{G}(\Delta_T, \hat{a}_i) - \hat{G}_{Ri} \right) (\hat{a}_i - a_0) \right| : \hat{a}_i \geq a_0, \tilde{G}(\Delta_T, \hat{a}_i) - \hat{G}_{Ri} \leq 0, (\hat{a}_i, \hat{G}_{Ri}) \in \mathcal{D}_R \right\}.$$

and once again $a^*(\Delta_T, a_0) = \hat{a}_{i^*}$. Note that in (28) the crack arrest/propagation condition is directly imposed within the minimization procedure. In all cases, once a^* is known, Δ and P can be computed directly:

$$(29) \quad \Delta = \frac{C(a^*)}{C(a^*) + C_M} \Delta_T, \quad P = \frac{\Delta}{C(a^*)}.$$

Within an incremental loading procedure, we perform either global or local minimization to compute the equilibrium crack length a_{k+1} for given displacement $\Delta_{T k+1}$ at time t_{k+1} and crack length a_k at time t_k . Finally, we can compute Δ_{k+1} and P_{k+1} directly. More details are given in the next subsection.

3.3. Numerical implementation. This section provides more details on how the data-driven solution of the fracture problem is implemented within an incremental loading procedure. The applied displacement is parameterized as $\Delta_{T k} = \delta_T k$ where k is the load step number and δ_T the load step increment. The aim is then, given the current imposed displacement $\Delta_{T k+1}$ and the previous crack length a_k , to find within the material set \mathcal{D}_R the state that fulfils the global or local data-driven criteria described in Sect. 3.2. In this context, the variable a acts as a history variable, that is trivially initialized to the length of the initial crack a_0 .

Both global and local minimization need to be constrained by the irreversibility condition. A convenient way to enforce this constraint is to *a priori* restrict the minimization procedures to the states for which $a_{k+1} \geq a_k$ is fulfilled. Alternatively, one can adopt a reference system attached to the crack tip and reformulate the minimization problems in terms of crack length increments $\Delta a_{k+1} \geq 0$, a choice which makes the data set independent on the geometry and test setup.

In the following it is assumed that the material data set is sufficient to study the problem at hand, meaning that the points in \mathcal{D}_R cover the propagation of the crack from the initial length a_0 to the maximum extension allowed by the geometry and setup under investigation.

3.3.1. Global minimization. Algorithm 1 presents the procedure to obtain the data-driven solution of the crack propagation problem as the global minimum of the function $\tilde{\Phi}(\Delta_T, a)$. Note that, if the material data set contains

no point with $\hat{a} = a_0$, at the first load step the minimization procedure always predicts crack propagation, and the extent of this propagation depends on the characteristics of the data set \mathcal{D}_R .

The global minimization procedure does not detect the occurrence of unstable crack propagation and keeps delivering a (possibly constant) solution state.

Algorithm 1: Data-driven fracture mechanics algorithm - global minimization. Given: $\tilde{E}(\Delta_T, a)$, $C(a)$, \mathcal{D}_R .

1 **Step** : $k + 1$

Input: $\Delta_{T k+1}$, a_k

Output: a_{k+1} , Δ_{k+1} , P_{k+1}

/* BEGINNING OF THE COMPUTATION

*/

2 **Define:** $\mathcal{D}_{R k+1} = \left\{ (\hat{a}_i, \hat{F}_{Ri}) \in \mathcal{D}_R : \hat{a} \geq a_k \right\}$

/* Compute the solution

*/

3 **Compute:**

$$i^*(\Delta_T, a_0) = \underset{i}{\operatorname{argmin}} \left\{ \tilde{E}(\Delta_T, \hat{a}_i) + \hat{F}_{Ri} : (\hat{a}_i, \hat{F}_{Ri}) \in \mathcal{D}_{R k+1} \right\}$$

$$a_{k+1} = \hat{a}_{i^*}$$

$$4 \Delta_{k+1} = \frac{C(a_{k+1})}{C(a_{k+1}) + C_M} \Delta_{T k+1}, \quad P_{k+1} = \frac{\Delta_{T k+1}}{C(a_{k+1}) + C_M}$$

3.3.2. *Local minimization based on closest point projection.* The implementation of the closest point projection strategy is detailed in Algorithm 2. This algorithm is slightly more complicated but it allows a deeper analysis. The history variables are both a and G_R and this allows to distinguish within the data-driven search procedure between an elastic step and a dissipative step. The related energy release rate quantities are collected in $G_{DD k+1}$. This seemingly redundant distinction can be exploited to implement a data-driven search also for the elastic step. This can be done by introducing an elastic material data set that accounts, e.g., for the measuring tolerance of the crack length. Moreover, this distinction reduces the computational time if requiring a data-driven search only when the propagation condition is met.

The quantity G_R triggers the crack propagation, hence, the initial crack increment depends on its initialization. If the initial crack length a_0 corresponds to a point of the material data set \mathcal{D}_R , then the couple (a_0, G_{R0}) can be trivially set to the coordinates of that point. Otherwise, one can set G_{R0} as the average value of \hat{G} of the two points in \mathcal{D}_R with value of \hat{a} immediately larger and smaller than a_0 or set G_{R0} to 0. With the former choice, adopted here, the computation involves an elastic branch from

the first load step that proceeds until $G(\Delta_T, a_0) \leq G_{R0}$, the latter choice instead predicts an initial increment of crack length similarly to what was noted for the global minimization approach.

Algorithm 2 entails the definition of a tolerance (*tol*) to be applied to the distance between the energy release rate function and the material data set. This allows to detect the occurrence of unstable crack propagation. The value of *tol* must be related to the characteristics of the data set and we suggest to set it to 5-10 times the average crack size increment in the adopted material data set.

Algorithm 2: Data-driven fracture mechanics algorithm - local minimization with closest point projection. Given: $\tilde{G}(\Delta_T, a)$, $C(a)$, \mathcal{D}_R .

```

1 Step :  $k + 1$ 
   Input :  $\Delta_{T k+1}, a_k, G_{Rk}$ 
   Output :  $a_{k+1}, G_{R k+1}, \Delta_{k+1}, P_{k+1}, G_{DD k+1}$ 
   /* BEGINNING OF THE COMPUTATION */
2 Define :  $\mathcal{D}_{R k+1} = \left\{ (\hat{a}_i, \hat{G}_{Ri}) \in \mathcal{D}_R : \hat{a}_i \geq a_k \right\}$ 
   /* Compute the solution */
3 if  $G_{Rk} > \tilde{G}(\Delta_{T k+1}, a_k)$  then // Elastic step
4 |   Assign :  $a_{k+1} = a_k, G_{Rk+1} = G_{Rk}, G_{DD k+1} = \tilde{G}(\Delta_{T k+1}, a_k)$ 
5 else // Dissipative step
6 |   Compute:
7 |    $\tilde{d}_i(\Delta_{T k+1}, a_k) = \min_{a \geq a_k} \left\{ \sqrt{(\hat{a}_i - a)^2 + (\hat{G}_{Ri} - \tilde{G}(\Delta_{T k+1}, a))^2} \right\}$ 
8 |    $i^*(\Delta_{T k+1}, a_k) = \underset{i}{\operatorname{argmin}} \left\{ \tilde{d}_i(\Delta_{T k+1}, a_k) : (\hat{a}_i, \hat{G}_{Ri}) \in \mathcal{D}_{R k+1} \right\}$ 
9 |   Assign :  $a_{k+1} = \hat{a}_{i^*}, G_{Rk+1} = \hat{G}_{Ri^*}, G_{DD k+1} = \hat{G}_{Ri^*}$ 
10 |  if  $\tilde{d}_{i^*}(\Delta_{T k+1}, a_k) > tol$  then
11 |  |   Unstable propagation  $\rightarrow$  EXIT // Specimen failure
12 |  end
13 end
14 Compute :  $\Delta_{k+1} = \frac{C(a_{k+1})}{C(a_{k+1}) + C_M} \Delta_{T k+1}, P_{k+1} = \frac{\Delta_{T k+1}}{C(a_{k+1}) + C_M}$ 

```

3.3.3. *Local minimization based on the consistency condition.* The implementation of the local minimization based on the consistency condition is detailed in Algorithm 3. Here, the solution of the problem given a certain displacement $\Delta_{T k+1}$ is defined as the point (\hat{a}, \hat{G}_R) that minimizes the violation of the consistency condition (20c). Such condition already encodes the propagation criterion and, hence, makes the definition of G_R redundant (although still possible) preventing the distinction between elastic and dissipative steps. In turn, this might lead, when a_0 is not represented in \mathcal{D}_R , to an increment of the crack size at the first load step, similarly to what mentioned for the closest point projection where G_R is initialized to 0. The restriction of the minimization to the points with $\hat{G}_R \geq \tilde{G}(\Delta_T, \hat{a})$ allows to detect unstable crack propagation without the introduction of any tolerance.

Algorithm 3: Data-driven fracture mechanics algorithm - local minimization with consistency condition. Given: $\tilde{G}(\Delta_T, a)$, $C(a)$, \mathcal{D}_R .

```

1 Step :  $k + 1$ 
   Input:  $\Delta_{T k+1}$ ,  $a_k$ 
   Output:  $a_{k+1}$ ,  $G_{R k+1}$ ,  $\Delta_{k+1}$ ,  $P_{k+1}$ 
   /* BEGINNING OF THE COMPUTATION */
2 Define:  $\mathcal{D}_{R k+1} = \left\{ (\hat{a}_i, \hat{G}_{Ri}) \in \mathcal{D}_R : \hat{a}_i \geq a_k, \hat{G}_{Ri} \geq \tilde{G}(\Delta_{T k+1}, \hat{a}_i) \right\}$ 
   /* Compute the solution */
3 if  $\mathcal{D}_{R k+1} \neq \emptyset$  then
4   Compute:
5      $i^*(\Delta_{T k+1}, a_k) = \underset{i}{\operatorname{argmin}} \left\{ \left| \left( \tilde{G}(\Delta_{T k+1}, \hat{a}_i) - \hat{G}_{Ri} \right) (a_k - \hat{a}_i) \right| : \right.$ 
6      $\left. (\hat{a}_i, \hat{G}_{Ri}) \in \mathcal{D}_{R k+1} \right\}$ 
7      $a_{k+1} = \hat{a}_{i^*}$ ,  $G_{R k+1} = \hat{G}_{R i^*}$ 
7 else
8   Unstable propagation  $\rightarrow$  EXIT // Specimen failure
9 end
10 Compute:  $\Delta_{k+1} = \frac{C(a_{k+1})}{C(a_{k+1}) + C_M} \Delta_{T k+1}$ ,  $P_{k+1} = \frac{\Delta_{T k+1}}{C(a_{k+1}) + C_M}$ 

```

4. NUMERICAL EXAMPLES

To demonstrate the capabilities of the proposed approach let us consider a double cantilever beam (DCB) with dimensions $L \times 2h \times b$ and initial crack length a_0 , whose arms are subjected to bending (Fig. 2). The test is

Young's modulus	Y	$=$	70 GPa
Height	h	$=$	3 mm
Length	L	$=$	30 mm
Thickness	b	$=$	1 mm
Initial crack length	a_0	$=$	3 mm
Displacement increment	δ_T	$=$	$1.5 \cdot 10^{-3}$ mm
Machine compliance	C_M	$=$	$2 \cdot 10^{-3}$ mm/N
Griffith fracture toughness (Reference)	γ	$=$	0.06 N/mm

TABLE 1. Parameters used for the computations.

performed imposing the loading device displacement Δ_T (Fig. 2) following a load ramp $\Delta_{T_k} = \delta_T k$. If not otherwise specified, the parameters are those in Tab. 1.

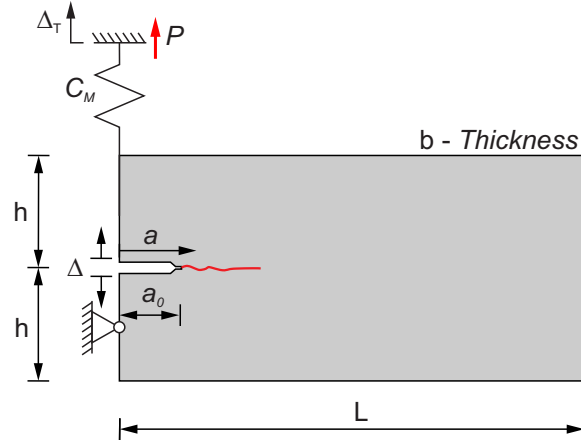


FIGURE 2. Scheme and geometry of the double cantilever beam test.

The following dimensionless quantities are used

$$\begin{aligned}
 \bar{L} &= \frac{L}{L} = 1, & \bar{h} &= \frac{h}{L}, & \bar{a} &= \frac{a}{L}, & \bar{b} &= \frac{b}{L}, \\
 \bar{C}_M &= C_M \gamma, & \bar{Y} &= \frac{YL}{\gamma}, & \bar{\Delta}_T &= \frac{\Delta_T}{L}, & \bar{\Phi} &= \frac{\Phi}{\gamma L^2}, \\
 \bar{G} &= \frac{G}{\gamma}, & \bar{E} &= \frac{E}{\gamma L^2}, & \bar{G}_R &= \frac{G_R}{\gamma}, & \bar{F}_R &= \frac{F_R}{\gamma L^2}.
 \end{aligned}
 \tag{30}$$

where the Griffith critical energy release rate γ should be intended as a reference value. For the geometry reported in Fig. 2, the dimensionless energy release rate is

$$(31) \quad \bar{G}(\bar{\Delta}_T, \bar{a}) = 12\bar{a}^2\bar{Y}\bar{h}^3 \left[\frac{\bar{\Delta}_T}{8\bar{a}^3 + \bar{C}_M\bar{Y}\bar{b}\bar{h}^3} \right]^2,$$

while the dimensionless compliance $\bar{C}(\bar{a})$ and applied load $\bar{P}(\bar{\Delta}_T, \bar{a})$ are

$$(32) \quad \bar{C}(\bar{a}) = \frac{8\bar{a}^3}{\bar{Y}\bar{b}\bar{h}^3}, \quad \bar{P}(\bar{\Delta}_T, \bar{a}) = \frac{\bar{\Delta}_T}{\bar{C}(\bar{a}) + \bar{C}_M}.$$

The introduction of a loading device has a twofold effect: on one hand it better represents the real testing conditions, on the other hand it provides a test control that is intermediate between the unstable P -driven test and the stable Δ -driven test. This results in a non-convex free energy function leading to an equilibrium states domain that includes an unstable branch for short cracks and a stable branch for longer cracks.

The data sets used in this paper are generated artificially to mimic different standard resistance models.

In the following, the data-driven results obtained using either Algorithm 1 or Algorithms 2-3 are compared with the reference solution of the global and local minimization problem, respectively. Global minimization is performed numerically at each time step by evaluating (17) at 1000 equispaced points along the interval $[0, \bar{L} = 1]$ and finding the solution with (19). The local minimizer is obtained analytically solving (11). In this case the possible occurrence of crack jumps and their position is not uniquely defined. However, to determine them one can invoke causality or Onsager's principle. This discussion is out of the scope of this paper but the interested reader can refer to [20, 21]. It is also worth mentioning that, for the case at hand, the globally stable states domain provides, in absence of initial defects, a finite crack nucleation load. Conversely, the local minimality condition forbids crack nucleation at finite loads in agreement with Griffith's theory.

4.1. Griffith fracture. In this section we present the results obtained using Griffith model, for which

$$(33) \quad \bar{G}_R = 1,$$

and

$$(34) \quad \frac{\bar{F}_R}{\bar{b}} = \bar{G}_R\bar{a} = \bar{a},$$

in terms of critical energy release rate and critical energy, respectively. The data sets used for the data-driven solution are obtained through a sampling of (33) and (34) with 50 points randomly distributed along the interval $\bar{a} = [0, 1.1\bar{L}]$. To allow a fair comparison between the different approaches, (33) and (34) are sampled at the same values of \bar{a} .

4.1.1. *Global minimization.* Fig. 3a shows the comparison between the reference and data-driven (DD in the figures) solution obtained using the global minimization approach (Algorithm 1) and the material data set shown in Fig. 3b.

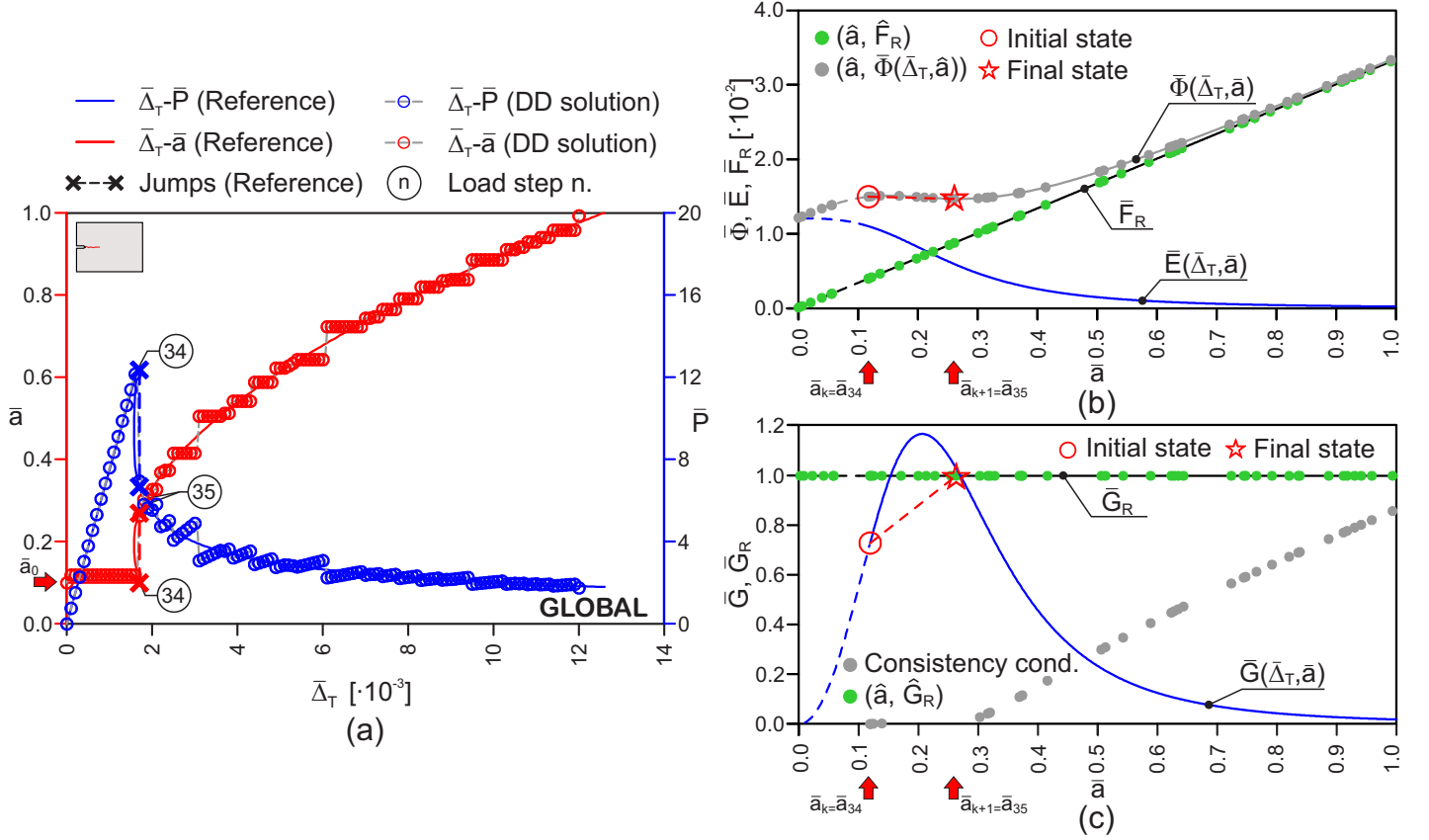


FIGURE 3. Data-driven results for Griffith fracture using global minimization: comparison between reference and data-driven results (a), data-driven search procedure at load step 35 (i. e., at the crack jump) in terms of energy (b) and of energy release rate (c).

Considering the limited number of data points used and the presence of large unsampled intervals of crack length (Figs. 3b,c), the agreement between reference and data-driven solution is excellent although the crack length undergoes a small increment already at the first load step (Fig. 3a) which is not present in the reference solution. This happens because there is no material data point for a crack length equal to \bar{a}_0 and, thus, the first data-driven search returns the closest globally stable point fulfilling the irreversibility condition.

Notably, the reference curve predicts a crack jump at the load step 35, i. e., for a machine displacement $\bar{\Delta}_T = 1.75 \cdot 10^{-3}$, which is correctly reproduced by the data-driven solution in terms of both position and extension although no ad-hoc criterion is introduced in Algorithm 1 (Fig. 3a). Fig. 3b shows the main energetic quantities at this load step, which can be taken as a paradigmatic example for the data-driven global minimization procedure. Here, it can be appreciated how the energy $\bar{E}(\bar{\Delta}_T, \bar{a})$ and the resistance energy term \bar{F}_R are composed in order to obtain the data set $\{\hat{a}_i, \bar{\Phi}(\bar{\Delta}_T, \hat{a}_i)\}$, on which minimization is performed to obtain the globally stable state at this load step. Figs. 3a and 3b show $\bar{a}_k = \bar{a}_{34}$, i. e., the crack length at the previous load step 34, which corresponds to the initial unstable state, as well as the computed crack length solution for the current load step $\bar{a}_{k+1} = \bar{a}_{35}$.

The crack jump in Fig. 3a is due to an unstable branch in the crack evolution curve which is the result of the non-convexity of the free-energy function. In particular, the initial value of the crack length \bar{a}_0 lies within an ascending branch of the free energy (Fig. 3a) part of which is inaccessible due to the irreversibility constraint (dashed line in Fig. 3b,c). This initial value corresponds to the global minimum of the accessible part of the function $\bar{\Phi}(\bar{\Delta}_T, \bar{a})$ until the device displacement $\bar{\Delta}_T = 1.75 \cdot 10^{-3}$, when the global minimum of the function suddenly changes its position from $\bar{a} = \bar{a}_0$ to $\bar{a} \simeq 0.27$. This forces the crack to extend until $\bar{a} \simeq 0.27$, which is seen by the system as a more favorable state. The finite increment of crack length induces an abrupt change in the compliance of the specimen triggering a snap back in the load-displacement curve (Fig. 3a). From a physical standpoint the crack jumps are the manifestation of dynamic effects not captured by the rate-independent quasi-static framework [22]. Fig. 3b shows also that, adopting a global minimality principle, in both data-driven and reference solution the state of the system at the crack jumps is allowed to overcome arbitrarily large energetic barriers violating the causality principle, as mentioned in sect. 2.1 and discussed in [20, 21].

For comparison purposes, the load step 35 is represented in terms of energy release rate in Fig. 3c, where we can observe that the initial state cannot be considered unstable from the standpoint of (11). This is a direct consequence of the globally stable domain being smaller compared to the domain of the locally stable states, as discussed in [20, 21]. Fig. 3c also reports the set of candidate points for the local minimum of Algorithm 3 (set $\mathcal{D}_{Rk+1} = \mathcal{D}_{R35}$ in Algorithm 3). The solution point obtained with the global minimum algorithm is not included, i. e., this point is not a candidate for Algorithm 3, while it is a good candidate for Algorithm 2 as it is quite close to the curve $\bar{G}(\bar{\Delta}_T, \bar{a})$.

4.1.2. Local minimization. Figs. 4a and 5a compare the reference and data-driven solutions obtained using local minimization along with closest point projection (27) and the consistency condition (28), respectively. In both cases the material data set is the same as in Sect. 4.1.1.

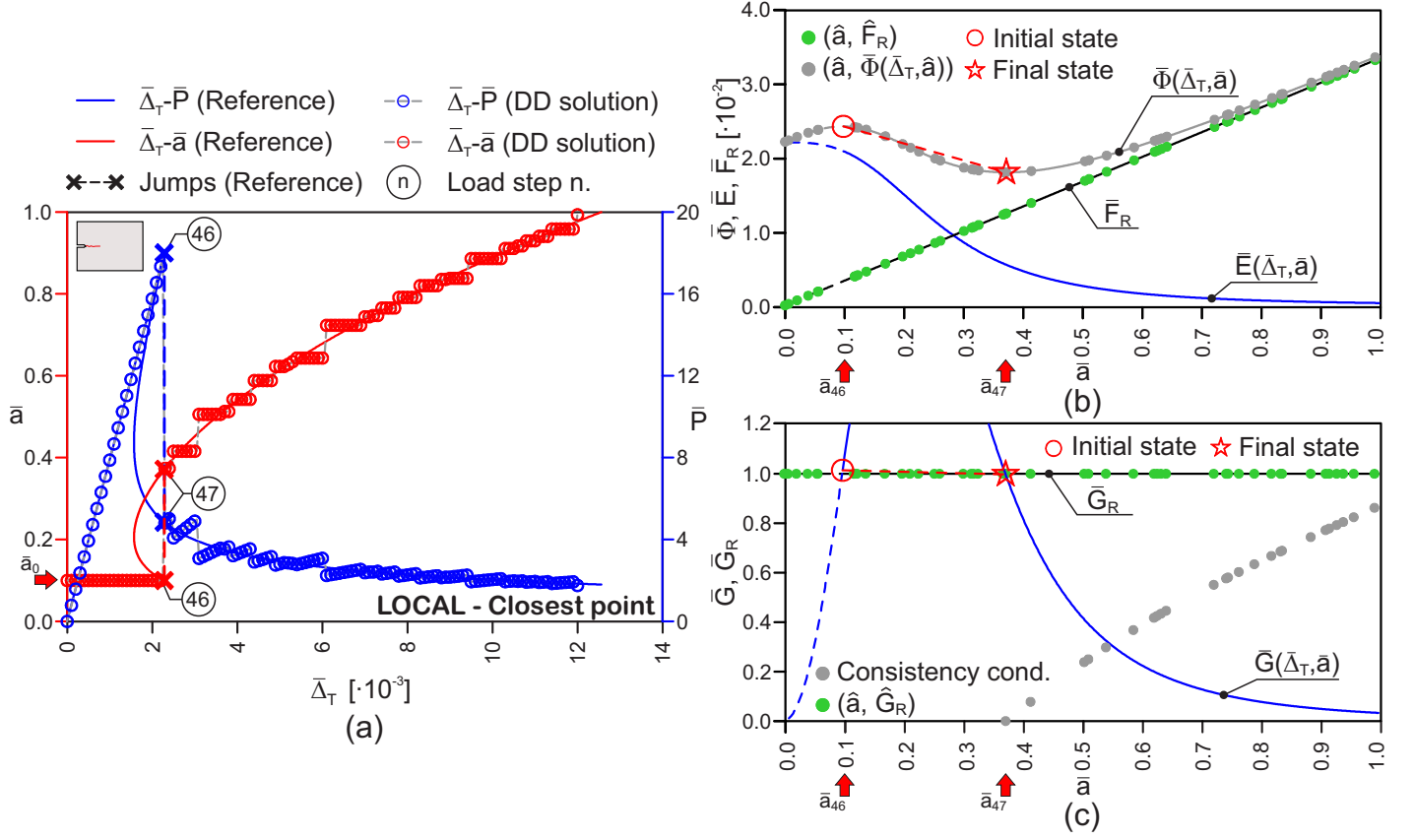


FIGURE 4. Data-driven results for Griffith fracture using local minimization and closest point projection: comparison between reference and data-driven results (a), data-driven search procedure at load step 47 (i. e., at the crack jump) in terms of energy (b) and of energy release rate (c).

Also in this case the reference solution involves a crack jump that takes place at $\bar{\Delta}_T = 2.23 \cdot 10^{-3}$. This value is higher than that obtained from global minimization, which is again consistent with the larger extension of the locally stable states domain [18, 20, 21]. Here the system does not evolve as long as there is an energetic barrier separating the current state and a more energetically favorable and accessible state. For a device displacement $\bar{\Delta}_T = 2.23 \cdot 10^{-3}$ the state corresponding to $\bar{a} = \bar{a}_0$ is surrounded by accessible states characterized by lower energies. This makes the current state unstable and leads to the next quasi-static equilibrium condition at $\bar{a} \simeq 0.37$, upon a finite crack size increment. This, once again, triggers a snap-back branch in the load-displacement curve. Also in this case dynamic effects can be advocated as underlying physical phenomenon that leads the system through a series of unstable states to a new (local) equilibrium condition [22]. The

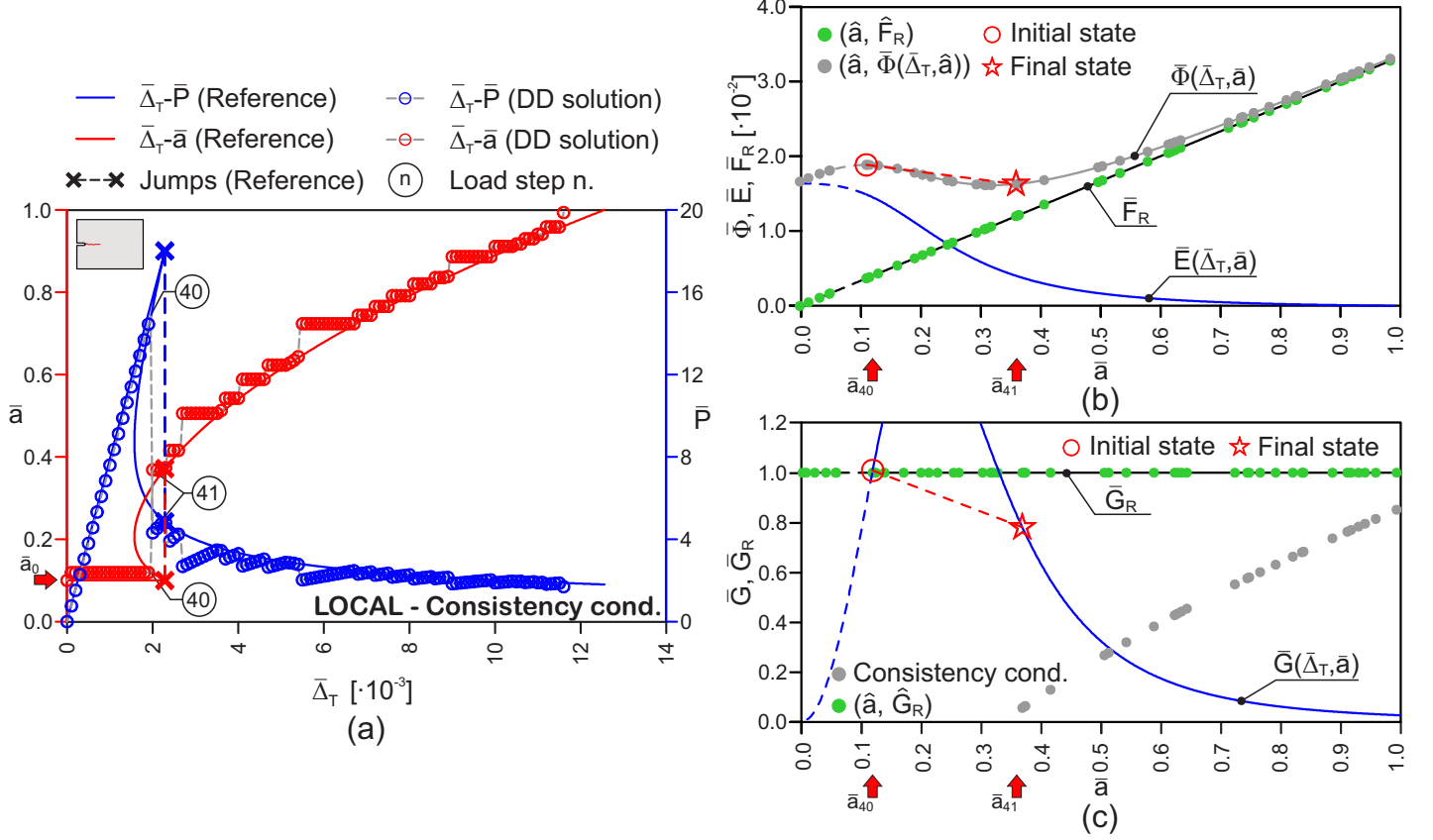


FIGURE 5. Data-driven results for Griffith fracture using local minimization and the consistency condition: comparison between reference and data-driven results (a), data-driven search procedure at load step 41 (i. e., at the crack jump) in terms of energy (b) and of energy release rate (c).

higher displacement attained before the crack jump also leads to a higher peak load, which is evident comparing Figs. 4a and 5a with Fig. 3a.

Once again the agreement between reference and data-driven solution is excellent. The data-driven search procedure based on closest point projection performs better than that based on the consistency condition, especially in predicting the peak load (Figs. 4a and 5a). This is mainly due to the fact that the latter undergoes a limited evolution of the crack length at the first load step (Figs. 5a) for the same reason highlighted for the global minimum solution in Sect. 4.1.1. This does not hold for the closest point projection procedure (Figs. 4a) because of the initialization of \bar{G}_R (Sect. 3.3.2), which is mostly responsible for the first evolution of the crack length. For this reason the two approaches predict the crack jump to take place at two different

load steps, namely at the 47th ($\bar{\Delta}_T = 2.35 \cdot 10^{-3}$) and 41st ($\bar{\Delta}_T = 2.05 \cdot 10^{-3}$) for the closest point projection and the consistency condition, respectively.

Figs. 4b,c and 5b,c illustrate the data-driven search procedure at the crack jump for the two approaches. Apart from the peak load, results are very similar. In particular, they are both consistent with the characteristic of local minimality of preventing the system from overcoming energetic barriers at the crack jump (Figs. 4b and 5b). The main difference is that the consistency condition strategy strictly enforces (11b), hence, it has the tendency to overestimate the crack length and to accept values of the energy release rate smaller than the critical one at the final state (Fig. 5c). Conversely, the closest point projection allows also values of energy release rate slightly larger than the critical one, hence, it alternates between over- and underestimations of the crack length (Fig. 4c).

4.1.3. Results in presence of noisy data. To determine the sensitivity of the proposed method to noise in the input data, a random white noise with amplitude $\pm 2.5\%$ in terms of difference between the observed and expected value is applied to the material data sets obtained by sampling (33) and (34). As before, sampling is performed at the same 50 values of crack lengths. Moreover, for consistency of both noisy data sets, points corresponding to the same values of crack length are affected by the same noise, i.e., for the same \hat{a}_i , the difference between expected and observed value of energy and energy release rate is the same. The results are illustrated in Figs. 6 to 8.

Comparing the results with and without noise, it is clear that data-driven global minimization is very sensitive to the presence of noise. The displacement vs. crack length curve involves several large crack jumps followed by long elastic branches (Fig. 6a). The data-driven search procedure related to the jump at load step 100 ($\bar{\Delta}_T = 5 \cdot 10^{-3}$) with global minimization is illustrated in Fig. 6b. Here the solution is seen to switch between points affected by large values of negative noise. In this case, this leads to an overestimation of the crack length delivering a solution point that refers clearly to an ascending branch of the reference noiseless total energy curve. From the standpoint of the energy release rate (Fig. 6c), this means that the solution often evolves from points clearly above to points clearly below the critical energy release rate.

The agreement between reference and data-driven results obtained with both local minimization procedures (Figs. 7a and 8a) is still excellent and comparable to that obtained in the noiseless case (Figs. 4a and 5a). The same observations of Sect. 4.1.2 apply. Figs. 7b,c and 8b,c illustrate the data-driven search procedures and the corresponding energetic quantities at the same load step analyzed for global minimization (Fig. 6b,c). Here we can see that the crack length for both local minimization strategies does not evolve. This is due to a relatively large unsampled interval of crack length, leading to a lack of better solution candidates than the values at load step 99. While with closest point projection the data-driven solution

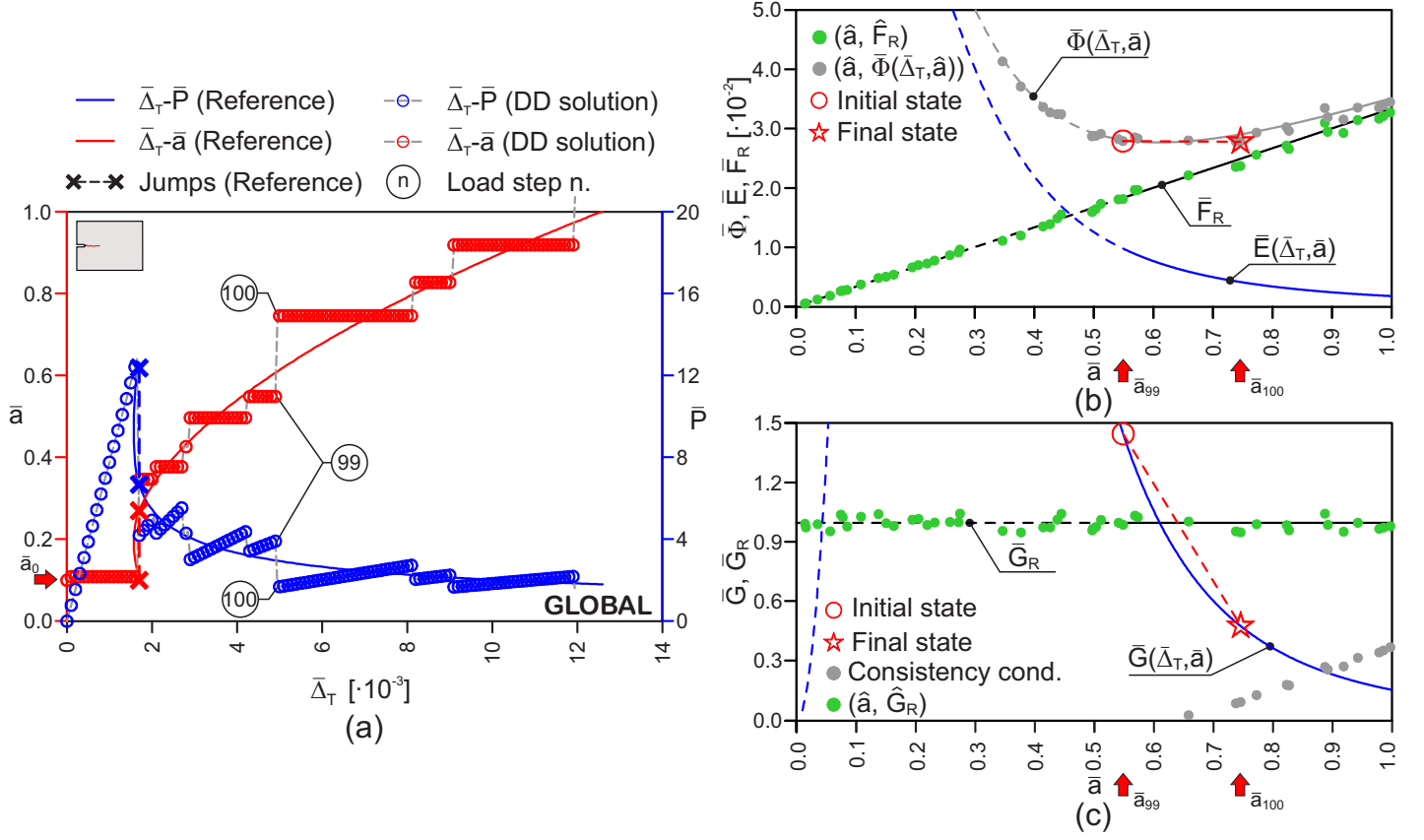


FIGURE 6. Data-driven results for Griffith fracture with a noisy material data set using global minimization: comparison between reference and data-driven results (a), data-driven search procedure at load step 100 in terms of energy (b) and of energy release rate (c).

underestimates the reference solution (Fig. 7a) because the energy release rate curve lies between two points of the data set (Fig. 7c), the consistency condition criterion overestimates the crack length (Fig. 8a,c). Nevertheless, in both cases the solution is close to the (local) minimum of the total energy (Figs. 7b and 8b).

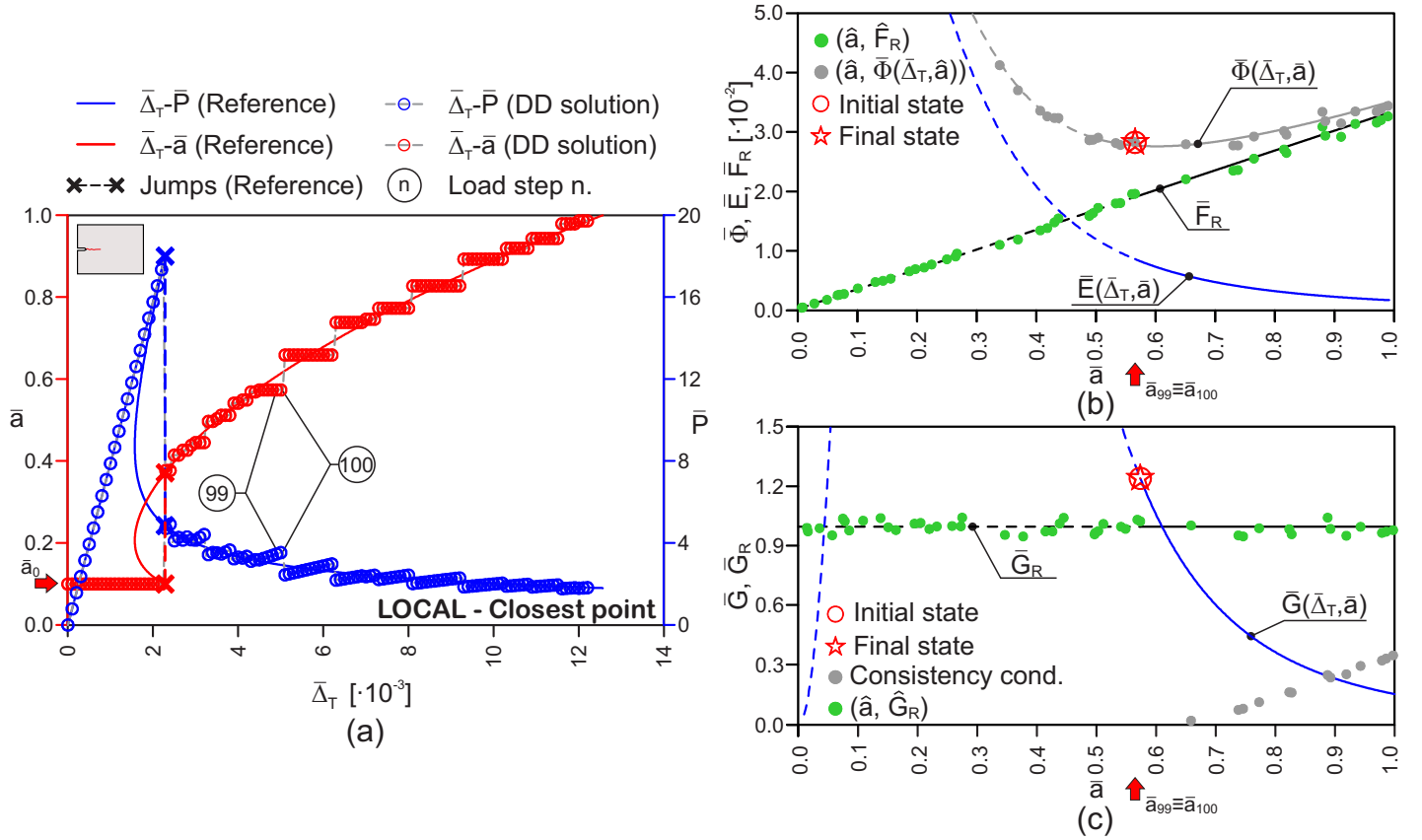


FIGURE 7. Data-driven results for Griffith fracture with a noisy material data set using local minimization and closest point projection: comparison between reference and data-driven results (a), data-driven search procedure at load step 100 in terms of energy (b) and of energy release rate (c).

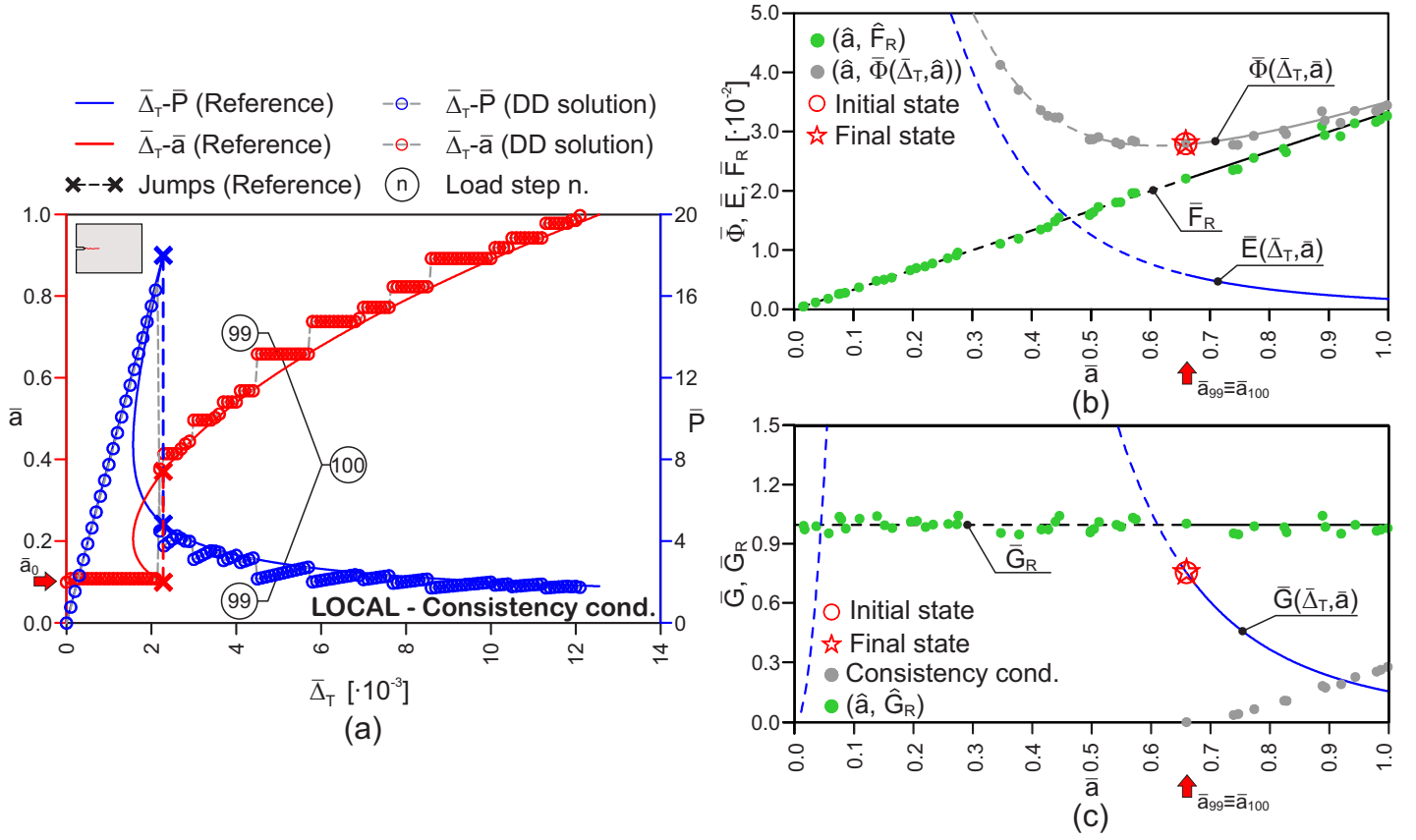


FIGURE 8. Data-driven results for Griffith fracture with a noisy material data set using local minimization and the consistency condition: comparison between reference and data-driven results (a), data-driven search procedure at load step 100 in terms of energy (b) and of energy release rate (c).

4.2. R-curve fracture. This section shows that the algorithms presented in Sect. 3.3 can be applied without any modification to other fracture models. We adopt the following R-curve model

$$(35) \quad \bar{G}_R(\bar{a}) = 1 + \frac{(\bar{a} - 0.1)^2}{(\bar{a} - 0.1)^2 + 0.2(\bar{a} - 0.1)},$$

or, in terms of energy

$$(36) \quad \frac{\bar{F}_R(\bar{a})}{\bar{b}} = 0.2 \left[10\bar{a} - \ln \left(\frac{\bar{a} + 0.1}{0.1} \right) \right].$$

Unless otherwise specified here and in the following, a random noise with amplitude $\pm 2.5\%$ is added to the material data set, which is composed of 50 randomly distributed points. Moreover, the loading ramp now includes a complete unloading-reloading branch that starts at $\bar{\Delta}_T = 5 \cdot 10^{-3}$. The results obtained with global minimization are illustrated in Fig. 9, while those of local minimization with closest point projection are presented in Fig. 10. From now on, the local minimization results obtained with the consistency condition are not reported, as they are similar to those obtained with closest point projection.

Both approaches are able to correctly follow the unloading-reloading curve A-B-C-D, see Figs. 9a and 10a. In particular, the unloading and reloading phases B-C and C-D follow a linear elastic path along the displacement vs. load curve, while the crack length remains constant (Figs. 9b,c and 10b,c).

The agreement between reference and data-driven results is similar as in the example with Griffith fracture. In particular, the presence of noise significantly affects the accuracy of the global minimization approach (Fig. 9a), as evident e.g. in the post peak portion of A-B in Fig. 9a. Figs. 9b,c show that among all the available states, global minimization tends to prefer points affected by a negative noise, thus promoting lower total energy (Figs. 9b). In the current example this causes the data-driven procedure to highly overestimate the ultimate displacement, defined as the displacement corresponding to $\bar{a} = 1$. The reference solution predicts an ultimate displacement $\bar{\Delta}_T = 16.9 \cdot 10^{-3}$ while global minimization reaches the ultimate condition at F for $\bar{\Delta}_T = 35.3 \cdot 10^{-3}$ (the last portion of the curves is not shown in Fig. 9a). This is due to the negative noise that affects the data-driven solution point E preceding the one leading to the ultimate condition (Figs. 9b,c). The ultimate point F is affected by a positive noise. Hence, to allow the ultimate state to become a global minimum, a large amount of energy must be provided to the system. Conversely, the local minimization approach is not biased towards any specific set of points and can switch to the ultimate condition much earlier, namely already at point E (Figs. 10b,c).

As mentioned earlier, local minimization based on closest point projection is the only data-driven procedure able to differentiate between dissipative

and elastic steps. Such distinction is visible in Fig. 10c, where the initial and unloading-reloading linear elastic phases are evident.

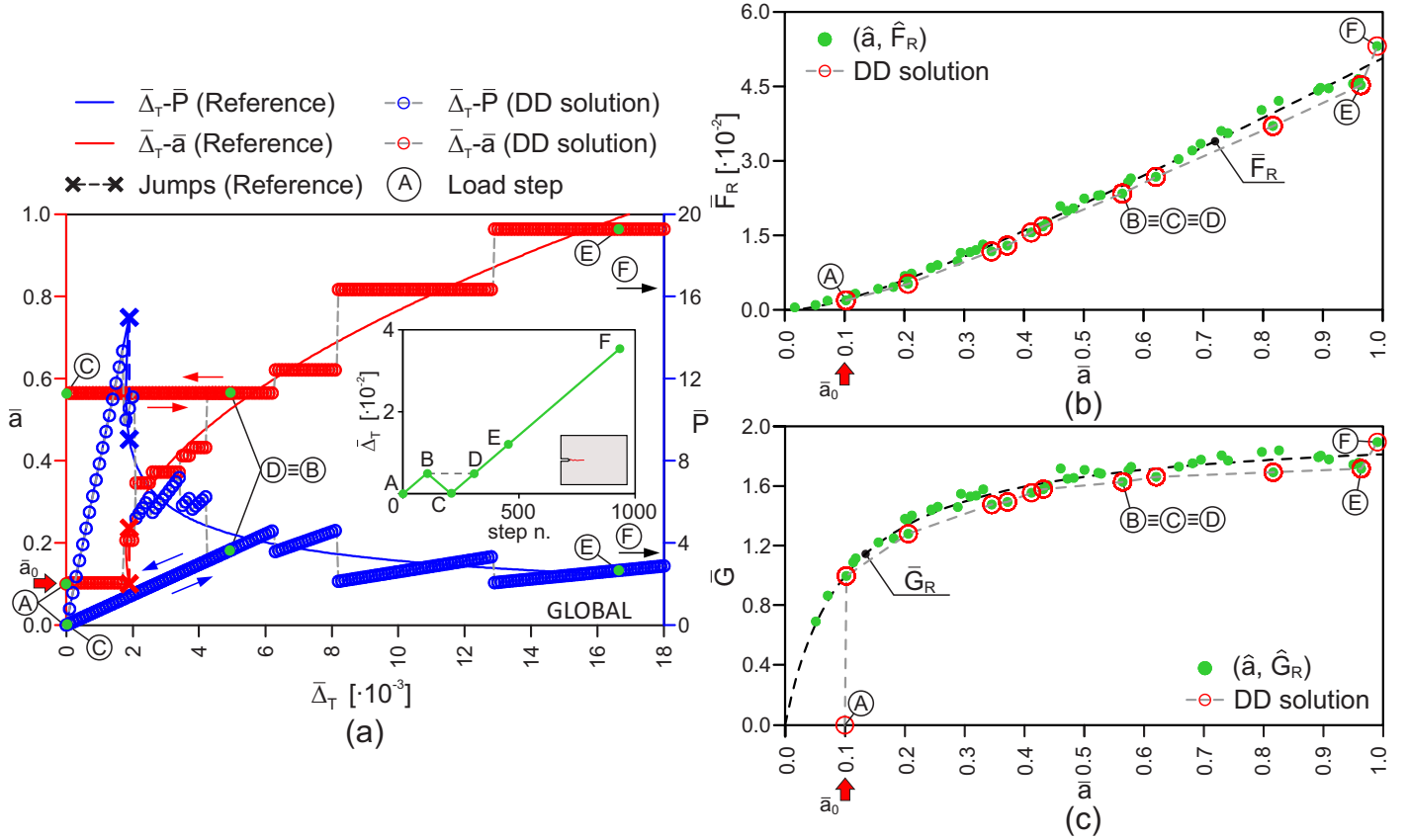


FIGURE 9. Data-driven results for an R-curve model with a noisy material data set using global minimization: comparison between reference and data-driven results (a), data-driven solution in terms of energy (b) and of energy release rate (c).

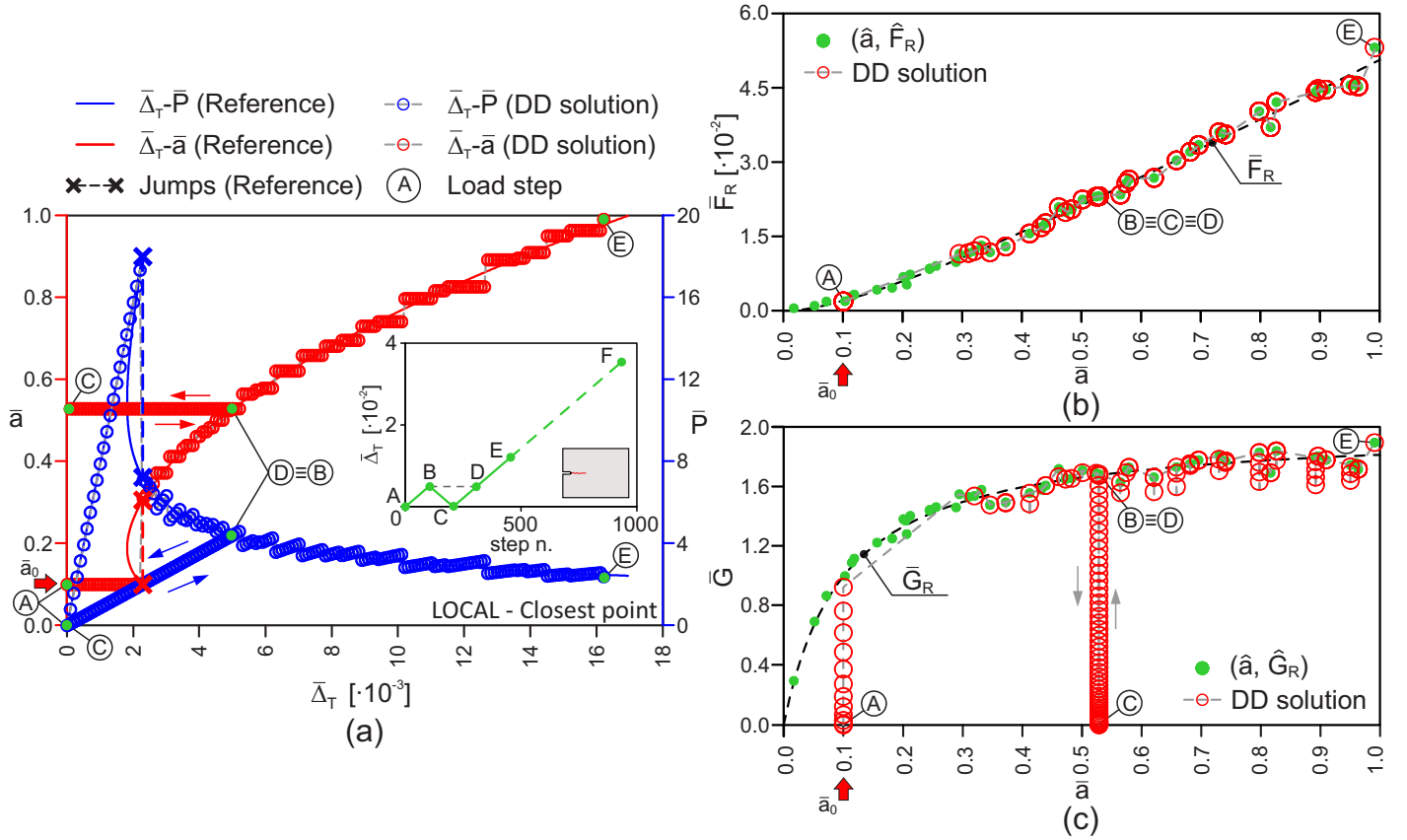


FIGURE 10. Data-driven results for an R-curve model with a noisy material data set using local minimization and closest point projection: comparison between reference and data-driven results (a), data-driven solution in terms of energy (b) and of energy release rate (c).

4.3. Bimaterial DCB. Let us now consider a DCB specimen composed of two different materials connected by a perfect interface (Fig. 11). The lengths of the two parts of the sample are $\bar{L}_1 = \bar{L}_2 = 0.5$ ($\bar{L}_i = L_i/L$). We model Griffith fracture with

$$(37) \quad \bar{G}_R(\bar{a}) = \begin{cases} 1 & \text{for } 0.0 < \bar{a} \leq 0.5 \\ 5 & \text{for } 0.5 < \bar{a} \leq 1.0, \end{cases}$$

or, in terms of energy

$$(38) \quad \frac{\bar{F}_R(\bar{a})}{\bar{b}} = \begin{cases} \bar{a} & \text{for } 0.0 < \bar{a} \leq 0.5 \\ (5\bar{a} - 2) & \text{for } 0.5 < \bar{a} \leq 1.0. \end{cases}$$

In this case, the crack must first traverse the weaker half of the sample to reach the strongest part, therefore this arrangement is termed *stable*. One can also define an *unstable* setup where the materials are reversed, i. e.,

$$(39) \quad \bar{G}_R(\bar{a}) = \begin{cases} 5 & \text{for } 0.0 < \bar{a} \leq 0.5 \\ 1 & \text{for } 0.5 < \bar{a} \leq 1.0, \end{cases}$$

or, in terms of energy

$$(40) \quad \frac{\bar{F}_R(\bar{a})}{\bar{b}} = \begin{cases} 5\bar{a} & \text{for } 0.0 < \bar{a} \leq 0.5 \\ (\bar{a} + 2) & \text{for } 0.5 < \bar{a} \leq 1.0. \end{cases}$$

Because of the drawbacks of global minimization discussed in the previous examples, from now on only local minimization is pursued. In Fig. 12a the reference and data-driven results obtained for the stable arrangement are compared and the agreement is very good. From the reference curves we can see that the crack stops propagating once it reaches the interface at $\bar{a} = 0.5$, until the energy release rate reaches the critical value of the strongest material. The data-driven solution is able to reproduce this behavior, however, due to the discrete set of states in the material data, the transition between the two halves of the specimen occurs approximately half way on the horizontal branch of the reference crack length vs. displacement curve, i. e., between the load steps A and B in Fig. 12. At this stage of the test the energy release rate curve is approximately at the same distance from the last available material point of the weakest and the first one of the strongest material (Fig. 12c). Since the transition occurs when the energy release rate is below the largest critical value, at the following load step C a linear elastic branch starts that persists until the evolution conditions are met again at load step D (Fig. 12b,c).

We now consider the *unstable* setup, whose results are presented in Fig. 13. The reference curves display two snap-backs, the first one at the peak load and the second one at $\bar{a} = 0.5$, i. e., when the crack tip reaches the interface.

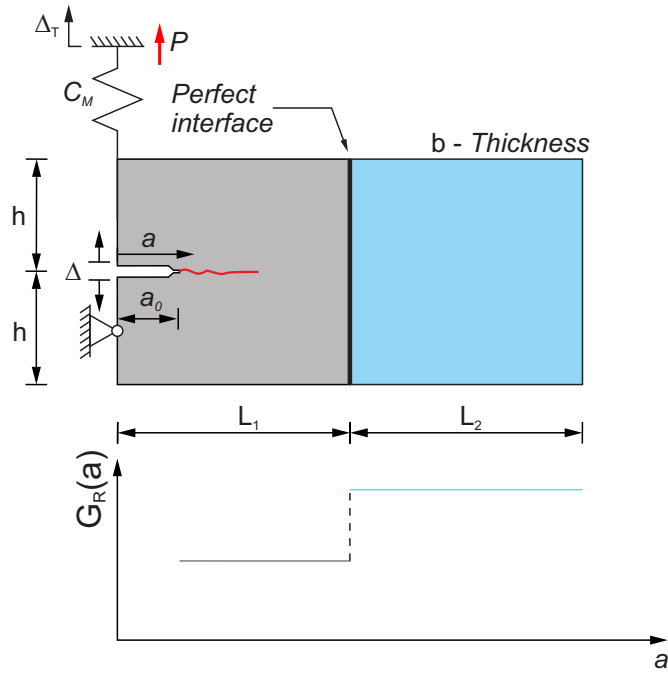


FIGURE 11. Sketch of the bimaterial DCB specimen.

As shown in Fig. 13a the data-driven approach does not reproduce the two jumps corresponding to these snap-backs, but merges them into one large jump. After reaching the peak load the crack tip jumps directly to the weakest portion of the specimen, then it follows again the reference solution. This result is due to a competition between different possible states after the peak load, as illustrated in Fig. 13b,c. For the analytical solution one can invoke causality or Onsager's principle [20] to favor the higher branch of the reference solution after the peak over the lower branch taken directly by the data-driven response. However, these considerations play no role in the data-driven procedures (as a side note, similar results are obtained with global minimization and with local minimization using a consistency condition criterion - not shown).

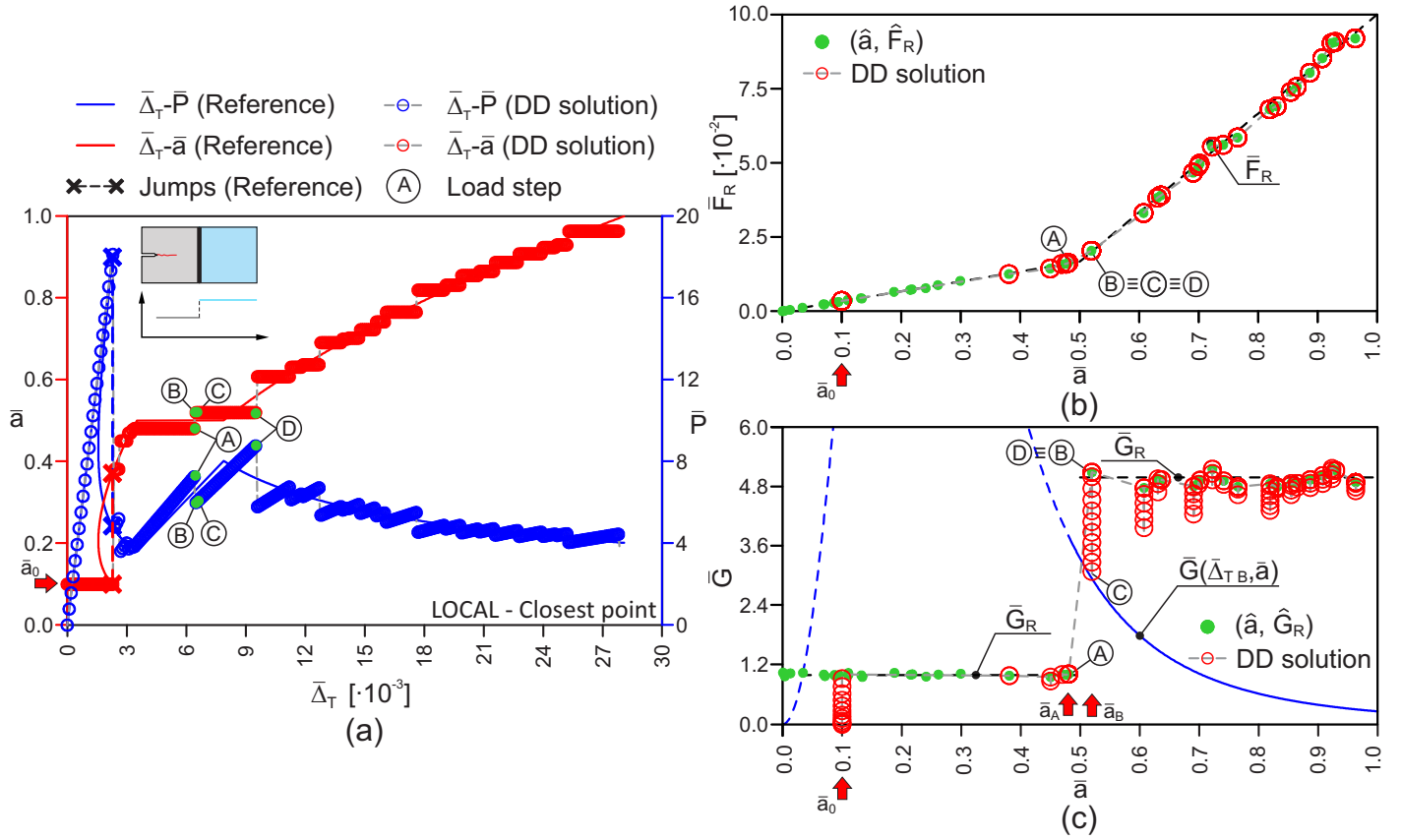


FIGURE 12. Data-driven results for the bimaterial DCB specimen (stable arrangement) using local minimization and closest point projection: comparison between reference and data-driven results (a), data-driven solution in terms of energy (b) and of energy release rate (c).

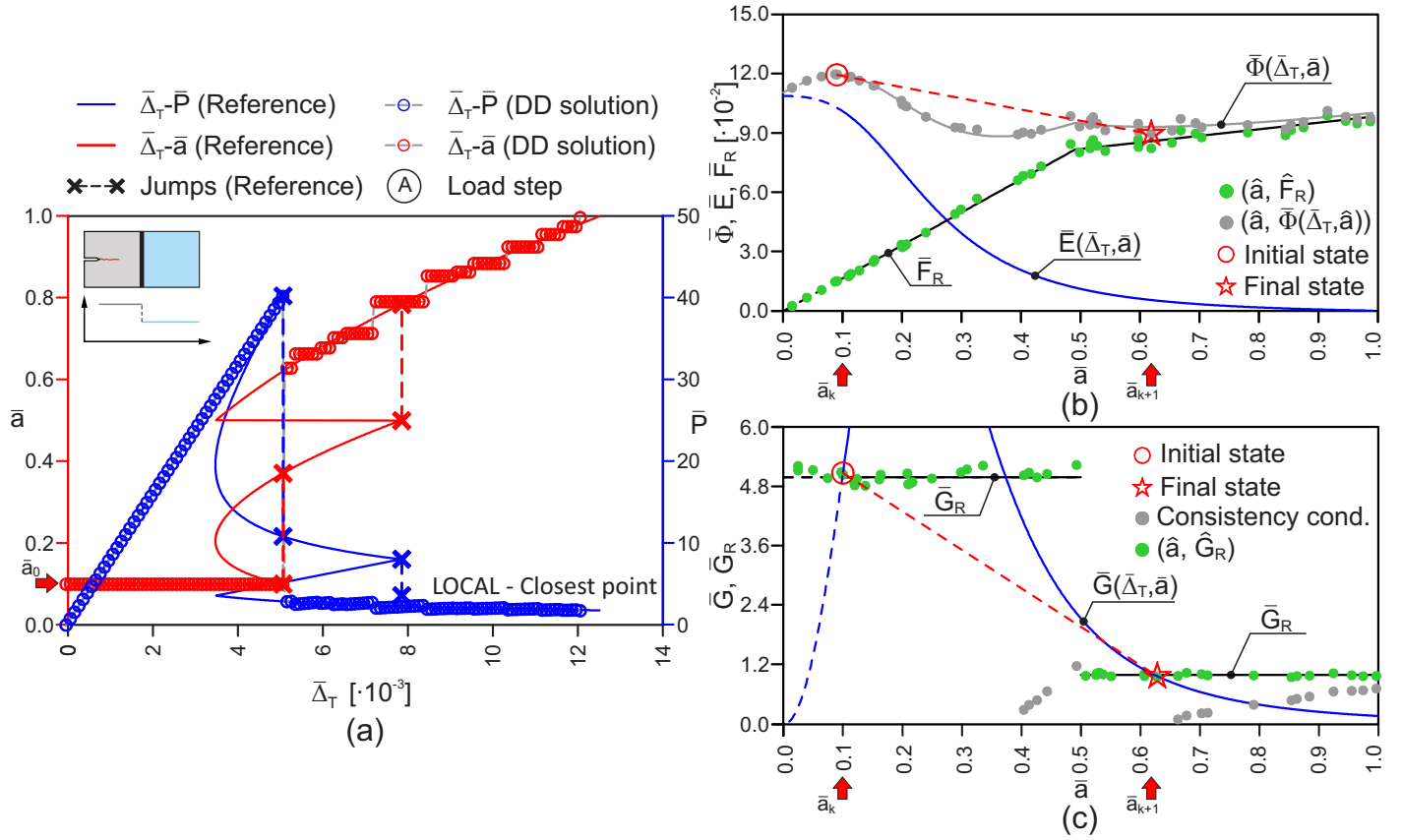


FIGURE 13. Data-driven results for the bimaterial DCB specimen (unstable arrangement) using local minimization and closest point projection: comparison between reference and data-driven results (a), data-driven search procedure at the load step corresponding to the crack jump in terms of energy (b) and of energy release rate (c).

4.4. Tapered DCB. In this section we analyze a homogeneous tapered DCB specimen, see Fig. 14. We assume the same Griffith model of Sect. 4.1, and the data set is composed of 100 points affected by random noise with amplitude $\pm 2.5\%$.

Unlike in the bimaterial DCB, here a transition in the cracking behavior is induced by the geometry of the specimen. The analytical compliance function is reported in Appendix A. As follows, three geometries are investigated, one with increasing height, and two with decreasing height and different slopes of the transition region, see Tab. 2.

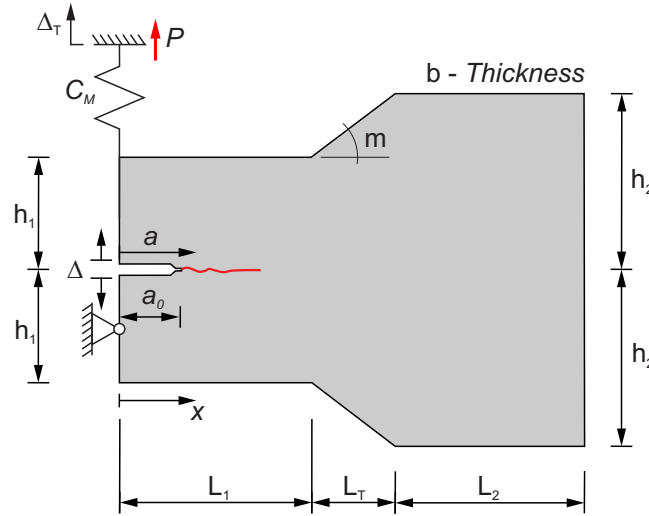


FIGURE 14. Sketch of the tapered DCB specimen.

As shown in Fig. 15, for the first two cases the results are similar as for the standard DCB. The reference solution features a snap-back whose position and extension is correctly reproduced by the data-driven results. In the third case the reference solution displays a second snap-back that takes place for

Parameter	CASE 1	CASE 2	CASE 3
\bar{h}_1	0.10	0.10	0.10
\bar{h}_2	0.15	0.05	0.04
\bar{L}_1	0.50	0.45	0.45
\bar{L}_T	0.10	0.30	0.10
\bar{L}_2	0.40	0.25	0.45
m ($^\circ$)	1/2 (26.56 $^\circ$)	-1/6 (-9.46 $^\circ$)	-3/5 (-30.96 $^\circ$)

TABLE 2. Parameters for the tapered DCB.

$\bar{a} = \bar{L}_1$. As for the bimaterial DCB with the unstable arrangement, the position of the second jump is clearly anticipated by the data-driven procedure (Fig. 16a). This is caused once again by the competition of different possible solution states, see Figs. 16b,c. After the second jump, the data-driven procedure goes back to closely reproducing the reference solution (Fig. 16a).

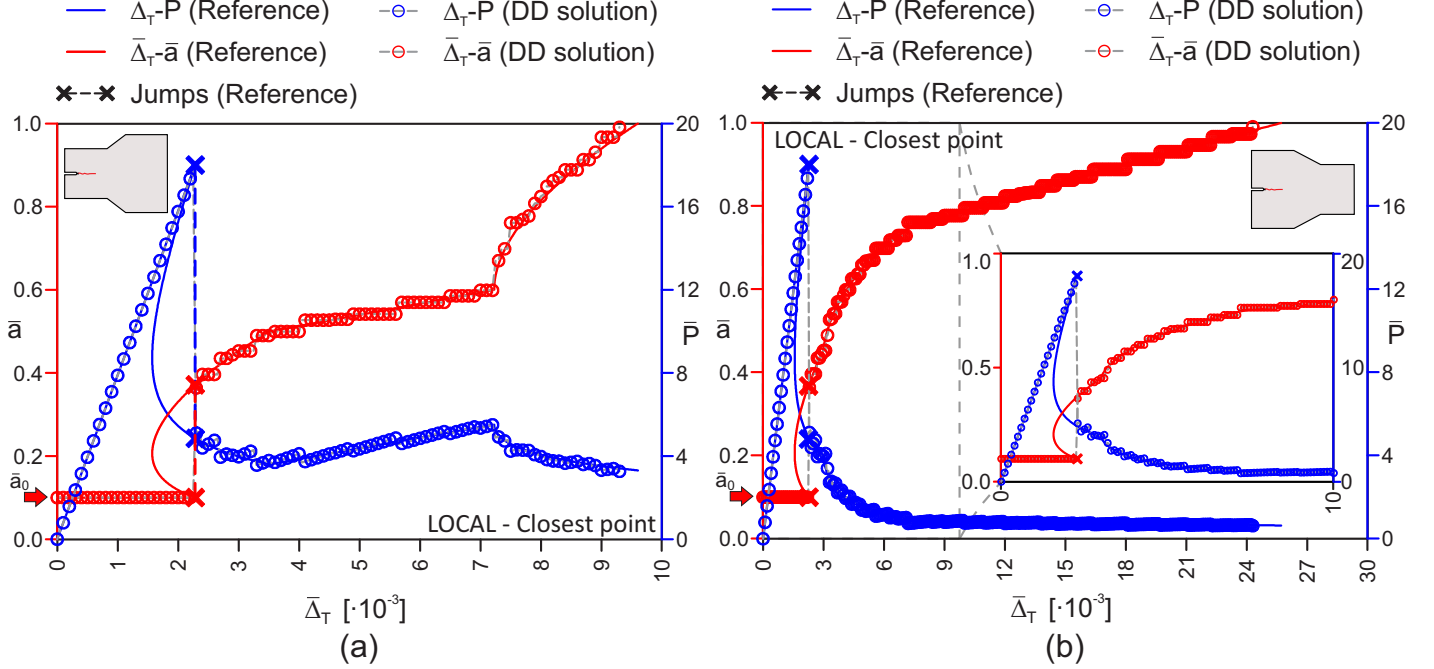


FIGURE 15. Comparison between reference and data-driven results for the tapered DCB specimen: CASE 1 (a) and CASE 2 (b).

4.5. Convergence. Aim of this section is to demonstrate convergence of the data-driven results to the reference solution with respect to the number of points in the material data set and the noise amplitude for both global and local minimization algorithms. To this end, we consider a DCB test for a Griffith material as in Sect. 4.1 and we compute the error ε of the data-driven solution with respect to the reference solution as

$$(41) \quad \varepsilon = \sqrt{\sum_{k=1}^N (\bar{a}_k - \bar{a}_k^{ref})^2},$$

where \bar{a}_k and \bar{a}_k^{ref} are respectively the data-driven and the reference solution computed for the same value of machine displacement $\bar{\Delta}_{T k}$. For each case considered in the following, we compute the average μ and the standard

deviation of the error for 100 solutions obtained changing the randomly sampled material database and, if applicable, the random noise. We also compute the frequency histograms of the error (in the range $[0, 2\mu]$ with bin size of 0.1μ) and the data-driven solution range of the \bar{a} vs. $\bar{\Delta}_T$ curve. The latter is the smallest area in the $\bar{\Delta}_T - \bar{a}$ plane that includes all the 100 data-driven solutions. The load step size is the same adopted in the previous sections, namely $\delta_{\bar{\Delta}_T} = 5 \cdot 10^{-5}$.

Fig. 17 show the results of the convergence study with respect to the number of points in a noiseless dataset. The average error is reported for 10, 20, 50, 100, 250, 500, 1000, 5000, and 10000 points. We can observe that for all approaches the rate of convergence is almost linear, with the closest point projection algorithm performing better than the other two. The

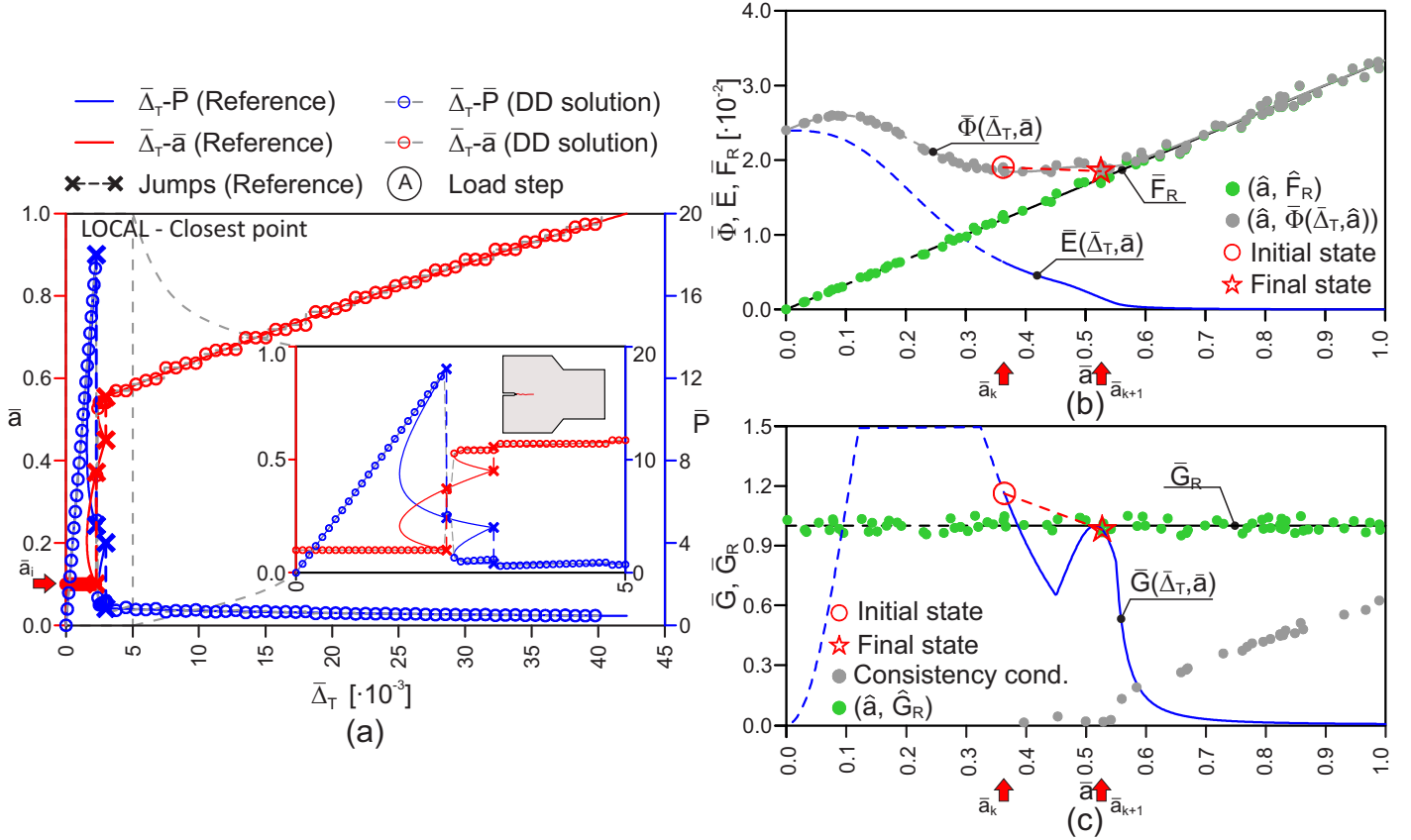


FIGURE 16. Data-driven results for the tapered DCB specimen (CASE 3) using local minimization and closest point projection: comparison between reference and data-driven results (a), data-driven search procedure for the load step corresponding to the second crack jump in terms of energy (b) and of energy release rate (c).

consistency condition approach features an initially lower convergence rate, due to a relatively high error contribution given by the crack propagation at the first load step when the initial crack length is not (even approximately) resolved within the dataset. This causes a delayed or anticipated initial crack jump responsible for a major contribution to the error, whose amplitude is governed by the snap-back characteristics and roughly independent of the dataset properties. Because of this phenomenon, increasing the size of the dataset leads to the clustering of the solutions in two groups: one featuring an incorrectly predicted crack jump affected by a higher error and one where the initial crack length is closely resolved and the error is much lower. This can be clearly observed in the frequency histograms related to datasets with 250, 500 and 1000 points of Fig. 17. Increasing further the number of points in the dataset leads to an improved convergence rate and the error becomes close to that of the other two approaches. A similar phenomenon occurs for the global minimization approach, but in this case the snap-back branch is less pronounced and leads to smaller errors. A clustering of the results is still present in this case already from the 50-points dataset although with much lower frequencies. Moreover, the convergence rate for this approach degrades for very dense datasets (i. e., with more than 1000 points). The range of the solutions in Fig. 17 confirms that the local minimization approach based on the consistency condition systematically overestimates the crack length, while the other two methods alternate over- and under-estimations. Also, we can see that the range of the solutions for 5000 points is indistinguishable from the reference solution for all the approaches.

The results of the convergence study with respect to the noise amplitude are presented in Fig. 18 for a dataset with 5000 points and 20%, 10%, 5%, 1%, $10^{-1}\%$ and $10^{-2}\%$ (i. e., $\pm 10\%$, $\pm 5\%$, $\pm 2.5\%$, $\pm 0.5\%$, $\pm 5 \cdot 10^{-2}\%$ and $\pm 5 \cdot 10^{-3}\%$) noise ranges. For the closest point projection approach, the convergence behavior is linear up to a noise range of 5% and then becomes almost quadratic until the error reaches the value of the noiseless case. The convergence behavior of the consistency condition approach is very similar. Unlike in the noiseless case, in presence of noise also an underestimation of the crack length is possible. Compared to both local minimization approaches, the global minimization method features a much slower convergence. This is clearly confirmed by, e.g., the data-driven solution range for 5% noise, which is much wider than those coming from the local minimization approaches (Fig. 18). The noiseless limit is not approached even for a noise range of $10^{-2}\%$. This slower convergence stems from the tendency of this approach, already noted earlier, to select points with high negative noise and, hence, to systematically anticipate the selection of a certain crack length (Fig. 18). For this reason, the range of the data-driven solutions lies always above the reference solution (Fig. 18).

A final comment is devoted to the computational efficiency. Although this is not quantitatively shown here, the closest point projection method is the most efficient. The other two approaches are slower due to the need

of selecting points within the material data set which fulfill certain requirements. Note that in our implementation of all methods the material data set is not sorted with respect to the crack length nor efficient search algorithms are adopted. This reduces the computational speed but is consistent with the intention of the model-free data-driven philosophy not to manipulate the material data set in any way.

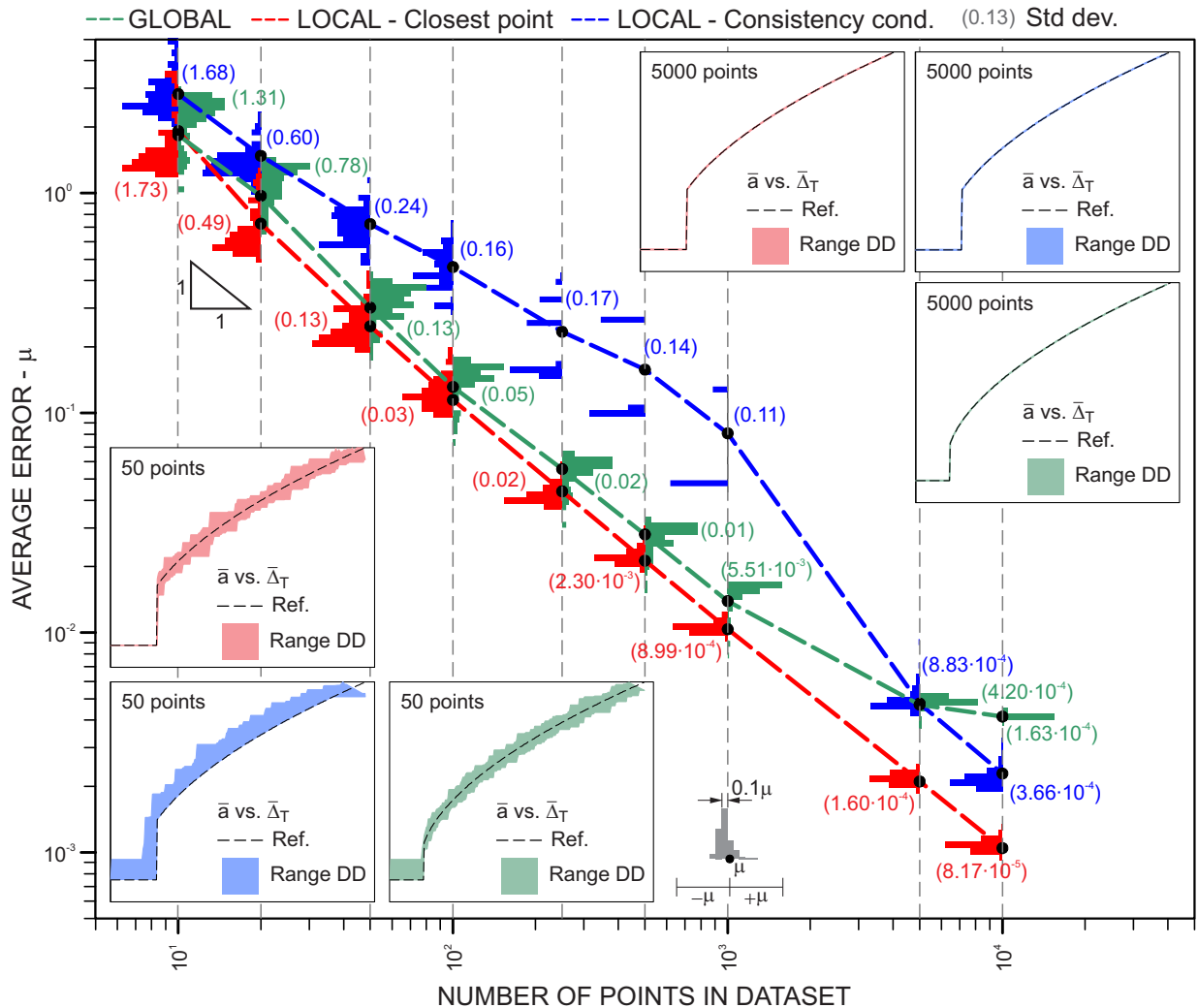


FIGURE 17. Convergence with respect to the number of points in the dataset including frequency histograms of the error and range of the solutions for 50 and 5000 points.

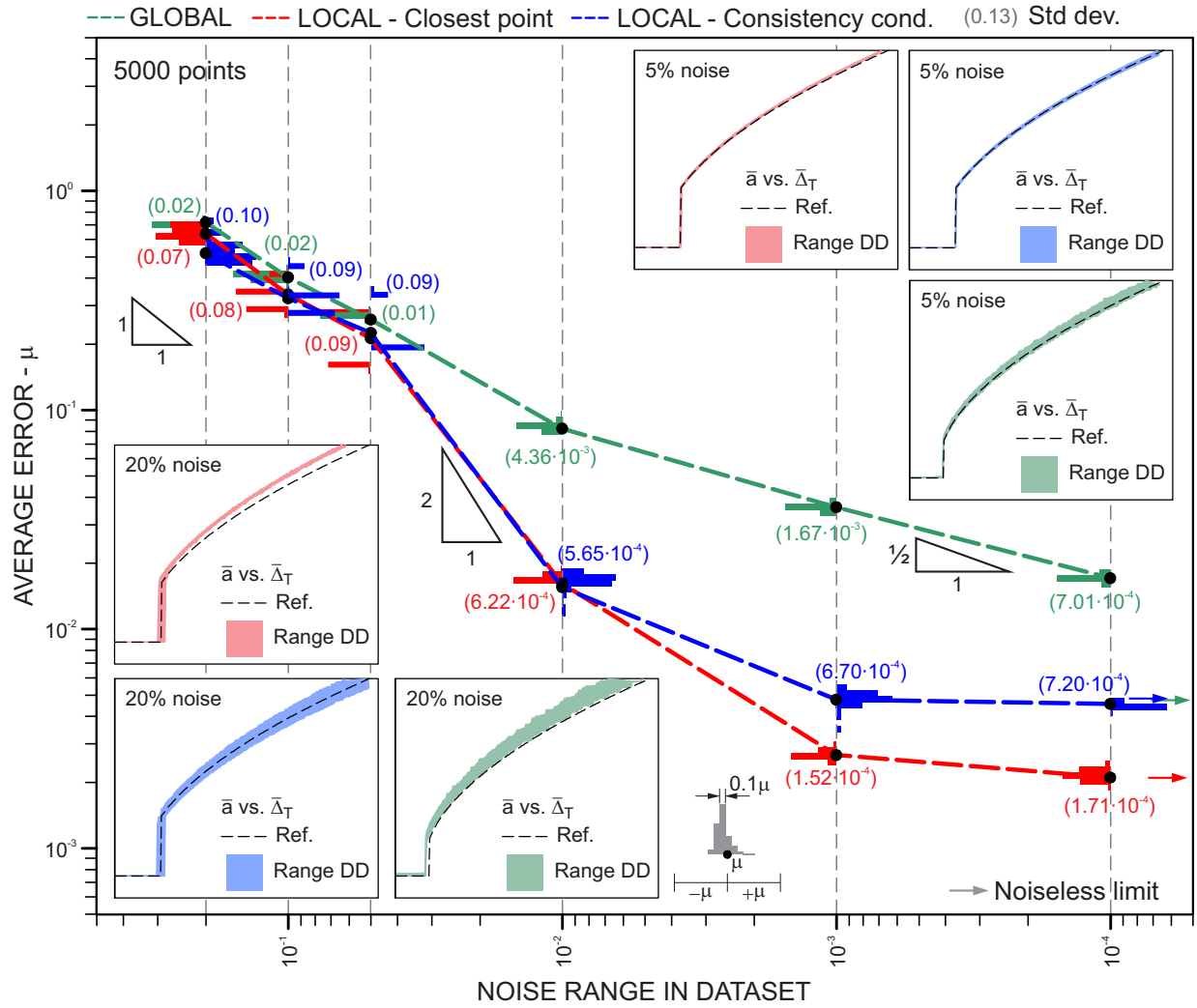


FIGURE 18. Convergence with respect to the noise amplitude in the dataset including frequency histograms of the error and range of the data-driven solutions for 20% (i. e., $\pm 10\%$) and 5% (i. e., $\pm 2.5\%$) noise amplitude.

5. SUMMARY AND CONCLUDING REMARKS

We have proposed a data-driven approach to rate-independent fracture mechanics in brittle materials. The main idea is to remove fracture-related material modeling assumptions from the formulation and let the fracture constitutive behavior be encoded exclusively in a discrete material data set, while simultaneously keeping the epistemic laws of fracture that stem from variational principles. Here we consider both solutions based on a metastability or local stability principle, fulfilling Kuhn-Tucker conditions for the energy release rate, and solutions based on a global stability principle corresponding to the minimization of the total free energy. The data-driven solution at a given load step is identified as the point within the data set that best fulfills either stationarity or global minimization of the free energy, leading to data-driven counterparts of both approaches. For local minimization, two alternative data-driven approaches are devised, one based on the closest-point projection of the material data set onto the (analytically known) energy-release rate function and another based on a consistency condition among data points that *a priori* satisfy the other two Kuhn-Tucker conditions. Both approaches have been tested on double-cantilever-beam examples with different geometries, using artificially generated material data sets, with or without random noise, which reproduce or randomize Griffith and R-curve type fracture models. A convergence study with respect of the number of points and the noise amplitude of the data set is also performed.

Based on the obtained results the following conclusions can be drawn:

- data-driven fracture mechanics approaches based on local or global stability deliver results in excellent agreement with those of their standard fracture mechanics counterparts. This implies in particular that the known drawbacks of global minimization (most notably, the possibility for the system to overcome energy barriers in case of crack jumps) are also observed in data-driven global minimization;
- the data-driven approaches based on local minimality feature an excellent robustness with respect to noisy data, whereas the quality of data-driven global minimization results is quite sensitive to noise;
- the two devised data-driven procedures based on local minimality deliver very similar results. The procedure based on closest point projection has the advantage of being able to automatically discriminate between crack arrest and crack propagation conditions, and is computationally less expensive;
- data-driven fracture mechanics is able to correctly reproduce crack jumps with no need for *ad hoc* criteria, provided that no competition takes place between different possible meta-stable states. Otherwise, the approach tends to select the state corresponding to the maximum dissipation;
- all proposed approaches deliver convergent results with respect to both the number of points in the data sets and the amplitude of a

random noise. The procedure based on local minimality and closest point projection features the best convergence rate.

ACKNOWLEDGEMENTS

P. Carrara gratefully acknowledges the financial support of the German Research Foundation (DFG) through the Fellowship Grant CA 2359/1.

REFERENCES

- [1] M. A. Bessa, R. Bostanabad, Z. Liu, A. Hu, Daniel W. Apley, C. Brinson, W. Chen, and Wing Kam Liu. A framework for data-driven analysis of materials under uncertainty: Countering the curse of dimensionality. *Computer Methods in Applied Mechanics and Engineering*, 320:633–667, 2017.
- [2] David E. Goldberg and Chie Hsiung Kuo. Genetic Algorithms in Pipeline Optimization. *Journal of Computing in Civil Engineering*, 1(2):128–141, apr 1987.
- [3] J. Ghaboussi, J. H. Garrett, and X. Wu. KnowledgeBased Modeling of Material Behavior with Neural Networks. *Journal of Engineering Mechanics*, 117(1):132–153, jan 1991.
- [4] S. Pernot and C.-H. Lamarque. Application of neural networks to the modelling of some constitutive laws. *Neural Networks*, 12(2):371–392, mar 1999.
- [5] T. Kirchdoerfer and Michael Ortiz. Data-driven computational mechanics. *Computer Methods in Applied Mechanics and Engineering*, 304:81–101, 2016.
- [6] E. Lopez, D. Gonzalez, J. V. Aguado, E. Abisset-Chavanne, E. Cueto, C. Binetruy, and F. Chinesta. A Manifold Learning Approach for Integrated Computational Materials Engineering. *Archives of Computational Methods in Engineering*, 25(1):59–68, jan 2018.
- [7] Lu Trong Khiem Nguyen and Marc André Keip. A data-driven approach to nonlinear elasticity. *Computers and Structures*, 194:97–115, 2018.
- [8] S. Conti, S. Müller, and M. Ortiz. Data-Driven Finite Elasticity. *Archive for Rational Mechanics and Analysis*, 237(1):1–33, jul 2020.
- [9] T. Kirchdoerfer and Michael Ortiz. Data-driven computing in dynamics. *International Journal for Numerical Methods in Engineering*, 113(11):1697–1710, 2018.
- [10] T. Kirchdoerfer and Michael Ortiz. Data Driven Computing with noisy material data sets. *Computer Methods in Applied Mechanics and Engineering*, 326:622–641, 2017.
- [11] Yoshihiro Kanno. Mixed-integer programming formulation of a data-driven solver in computational elasticity. *Optimization Letters*, 13(7):1505–1514, 2019.
- [12] Adrien Leygue, Michel Coret, Julien Réthoré, Laurent Stainier, and Erwan Verron. Data-based derivation of material response. *Comput. Methods Appl. Mech. Engrg.*, 331:184–196, 2018.
- [13] Laurent Stainier, Adrien Leygue, and Michael Ortiz. Model-free data-driven methods in mechanics: material data identification and solvers. *Computational Mechanics*, 64(2):381–393, aug 2019.
- [14] Ruben Ibañez, Domenico Borzacchiello, Jose Vicente Aguado, Emmanuelle Abisset-Chavanne, Elias Cueto, Pierre Ladeveze, and Francisco Chinesta. Data-driven nonlinear elasticity: constitutive manifold construction and problem discretization. *Computational Mechanics*, 60(5):813–826, 2017.
- [15] Ruben Ibañez, Emmanuelle Abisset-Chavanne, Jose Vicente Aguado, David Gonzalez, Elias Cueto, Jean Louis Duval, and Francisco Chinesta. A manifold learning approach to data-driven computational materials and processes. *AIP Conference Proceedings*, 1896, 2017.

- [16] Robert Eggersmann, Trenton Kirchdoerfer, Stefanie Reese, Laurent Stainier, and Michael Ortiz. Model-Free Data-Driven inelasticity. *Computer Methods in Applied Mechanics and Engineering*, 350:81–99, jun 2019.
- [17] Pierre Ladevèze, David Néron, and Paul-William Gerbaud. Data-driven computation for history-dependent materials. *Comptes Rendus Mécanique*, 347(11):831–844, 2019.
- [18] Matteo Negri and Christoph Ortner. Quasi-static crack propagation by Griffith’s criterion. *Mathematical Models and Methods in Applied Sciences*, 18(11):1895–1925, 2008.
- [19] Blaise Bourdin, Gilles A Francfort, and Jean-Jacques Marigo. The variational approach to fracture. *Journal of elasticity*, 91(1-3):5–148, 2008.
- [20] Matteo Negri. A comparative analysis on variational models for quasi-static brittle crack propagation. *Advances in Calculus of Variations*, 3(2):149–212, 2010.
- [21] Roberto Alessi. Energetic formulation for rate-independent processes: remarks on discontinuous evolutions with a simple example. *Acta Mechanica*, 227(10):2805–2829, 2016.
- [22] Matteo Negri. From Rate-Dependent to Rate-Independent Brittle Crack Propagation. *Journal of Elasticity*, 98(2):159–187, feb 2010.

APPENDIX A. COMPLIANCE FOR THE TAPERED DCB

Each arm of the tapered DCB specimen of Fig. 14 is assumed to behave as a cantilever beam whose length is equal to the crack extension a and loaded with a concentrated force P at the free end. The opening Δ of the tapered DCB is twice the free end deflection of the beam v_0 , so the compliance is directly computed from (1) as

$$(42) \quad C(a) = \frac{\Delta}{P} = \frac{2v_0}{P}.$$

Neglecting the shear contribution and the deformability of the uncracked portion of the specimen, the vertical displacement v can be computed integrating the Euler-Bernoulli beam equation

$$(43) \quad v''(x) = \frac{M(x)}{YI(x)} = \frac{12Px}{Ybh(x)^3} \quad \text{with} \quad I(x) = \frac{bh(x)^3}{12},$$

where $M(x)$ is the bending moment and $I(x)$ is the moment of inertia of the rectangular DCB section. With reference to Fig. 14 the following quantities are defined

$$(44) \quad p = h_1 - mL_1, \quad L_{1-2} = L_1 + L_T, \quad h_2 = h_1 + mL_T,$$

while the height reads

$$(45) \quad h(x) = \begin{cases} h_1 & \text{if } 0 < x \leq L_1 \\ p + mx & \text{if } L_1 < x \leq L_{1-2} \\ h_2 & \text{if } x > L_{1-2}. \end{cases}$$

To determine the integration constants, different kinematic boundary and continuity conditions are imposed as a function of the crack tip position, see Tab. 3.

The compliance function is given by

$$(46) \quad C(a) = \begin{cases} \frac{8a^3}{Ybh_1^3} & \text{if } 0 < a \leq L_1 \\ \frac{12}{Ybm^3} \left[\ln \left(\frac{ma+p}{mL_1+p} \right)^2 + \frac{p^2 - 2m^2a^2}{(ma+p)^2} + \right. \\ \quad \left. - \frac{p^2 - 2m^2L_1^2}{(mL_1+p)^2} + \frac{2m^3L_1^3}{3h_1^3} \right] & \text{if } L_1 < a \leq L_{1-2} \\ \frac{12}{Ybm^3} \left[\ln \left(\frac{mL_{1-2}+p}{mL_1+p} \right)^2 + \frac{p^2 - 2m^2L_{1-2}^2}{(mL_{1-2}+p)^2} + \right. \\ \quad \left. - \frac{p^2 - 2m^2L_1^2}{(mL_1+p)^2} + \frac{2m^3L_1^3}{3h_1^3} + \frac{2m^3(a^3 - L_{1-2}^3)}{3h_2^3} \right] & \text{if } a > L_{1-2}. \end{cases}$$

$0 < a \leq L_1$	$v_1(a) = v'_1(a) = 0$		
$L_1 < a \leq L_{1-2}$	$v_1(L_1) = v_T(L_1)$ $v'_1(L_1) = v'_T(L_1)$	$v_T(a) = v'_T(a) = 0$	
$a > L_{1-2}$	$v_1(L_1) = v_T(L_1)$ $v'_1(L_1) = v'_T(L_1)$	$v_T(L_{1-2}) = v_2(L_{1-2})$ $v'_T(L_{1-2}) = v'_2(L_{1-2})$	$v_2(a) = v'_2(a) = 0$

TABLE 3. Boundary conditions to determine the deflection of the tapered DCB specimen. Subscripts 1, 2 and T refer to the relationships obtained integrating (43) along L_1 , L_2 and L_T , respectively.

(P. Carrara*) DEPT. OF MECHANICAL AND PROCESS ENGINEERING, ETH ZÜRICH,
TANNENSTR. 3, 8092 ZURICH, SWITZERLAND
E-mail address: `pcarrara@ethz.ch`

(L. De Lorenzis) DEPT. OF MECHANICAL AND PROCESS ENGINEERING, ETH ZÜRICH,
TANNENSTR. 3, 8092 ZURICH, SWITZERLAND
E-mail address: `ldelorenzis@ethz.ch`

(L. Stainier) INSTITUT DE RECHERCHE EN GÉNIE CIVIL ET MÉCANIQUE (GEM - UMR
6183), ÉCOLE CENTRALE DE NANTES, 1 RUE DE LA NOË - BP 92101, 44321 NANTES
CEDEX 3, FRANCE.
E-mail address: `laurent.stainier@ec-nantes.fr`

(M. Ortiz) DIVISION OF ENGINEERING AND APPLIED SCIENCE, CALIFORNIA INSTITUTE
OF TECHNOLOGY, 1200 EAST CALIFORNIA BOULEVARD, PASADENA, CA 91125, USA.
E-mail address: `ortiz@caltech.edu`